

ABSTRACT

This project studied the flow field characteristics responsible for lateral instabilities observed on the F/A-18E/F in the Power Approach (PA) configuration. Discovered during the aircraft's initial testing, these instabilities were observed when the aircraft exceeded twelve degrees angle of attack, a behavior that came to be known as "PA wing drop." The problem was corrected by the closure of a vent on the aircraft body. However, neither the cause of the problem nor the mechanics of the solution was understood. This project used computational fluid dynamics to solve for the airflow properties over the aircraft with both the vent open and closed. Elements of the study included: 1) construction of a detailed computer model of the aircraft in both configurations; 2) generation of a computational grid encompassing the aircraft model and its surroundings; 3) computation of the airflow properties over the aircraft at different angles of attack; and 4) qualitative and quantitative analysis of the results. The project was performed in league with members of the Naval Air Systems Team, at Patuxent River, MD, and the NASA Langley Research Center.

Keywords: F/A-18 Hornet, computational fluids, wing drop

Form SF298 Citation Data

Report Date <i>("DD MON YYYY")</i> 08-05-2000	Report Type N/A	Dates Covered (from... to) <i>("DD MON YYYY")</i>
Title and Subtitle USNA Trident Scholar Project Report No. 274 (2000)	Contract or Grant Number	
	Program Element Number	
Authors Filbey, Joshua R.	Project Number	
	Task Number	
	Work Unit Number	
Performing Organization Name(s) and Address(es) U.S. Naval Academy Annapolis, MD	Performing Organization Number(s)	
Sponsoring/Monitoring Agency Name(s) and Address(es)	Monitoring Agency Acronym	
	Monitoring Agency Report Number(s)	
Distribution/Availability Statement Approved for public release, distribution unlimited		
Supplementary Notes Accepted by the U.S. Trident Scholar Committee		
Abstract This project studied the flow field characteristics responsible for lateral instabilities observed on the F/A-18E/F in the Power Approach (PA) configuration. Discovered during the aircrafts initial testing, these instabilities were observed when the aircraft exceeded twelve degrees angle of attack, a behavior that came to be known as PA wing drop. The problem was corrected by the closure of a vent on the aircraft body. However, neither the cause of the problem nor the mechanics of the solution was understood. This project used computational fluid dynamics to solve for the airflow properties over the aircraft with both the vent open and closed. Elements of the study included: 1) construction of a detailed computer model of the aircraft in both configurations; 2) generation of a computational grid encompassing the aircraft model and its surroundings; 3) computation of the airflow properties over the aircraft at different angles of attack; and 4) qualitative and quantitative analysis of the results. The project was performed in league with members of the Naval Air Systems Team, at Patuxent River, MD, and the NASA Langley Research Center.		
Subject Terms wing drop; F/A-18 Hornet; computational fluids		

Document Classification unclassified	Classification of SF298 unclassified
Classification of Abstract unclassified	Limitation of Abstract unlimited
Number of Pages 73	

ACKNOWLEDGMENTS

First off, I would like to thank Dr. Simha Dodbele and the rest of the NAVAIR 4.3.2.1 group. They put up with me for the summer and were there countless times when I had problems with the grid. Whether it was by e-mail or phone, Simha was there answering my questions and troubleshooting my grid. Without him and the NAVAIR team, I definitely would not have gotten anywhere.

Next I want to acknowledge the TetrUSS team at LaRC, specifically Stuart Pope and Dr. Paresh Parikh. Somehow over the course of the semester I discovered more errors and problems with my grid than either they or I ever thought possible; yet they were always there to help troubleshoot through.

I also want to thank Steve Cook, who came and talked with me numerous times about his work in the wind tunnel. He graciously lent me some of his results for validation of my work. Without his generosity, I would have nothing to back up my results.

Other groups of people who were instrumental in the success of this project included the CADIG staff at USNA, numerous NAVAIR and Boeing employees at Pax River, and the help desk at the NAVO computing office.

And of course, I want to thank CDR Niewoehner, my advisor, who even though he had the busiest schedule known to man, still always found time to be available and help me through the year. Whenever I had a question, he always had an answer, or was able to put me in touch with someone across the country who did know.

TABLE OF CONTENTS

Abstract	1
Acknowledgments	2
Table of Contents	3
List of Figures	4
List of Symbols	5
 I. Background	 6
1. LEX vent History	6
2. CFD Background	9
 II. Procedure	 14
1. Surface construction	15
2. Grid generation	17
3. Flow solution and analysis	20
 III. Test Equipment	 22
 IV. Model Generation	 22
1. Initial Geometry Selection	22
2. Model Challenges	24
3. Problem Areas	27
 V. Validation of CFD Model	 31
1. Wind Tunnel Results	31
2. Model Limitations	37
 VI. Results and Discussion	 41
1. Numerical data	41
2. Flow Visualizations	47
3. Summary of Results	56
 VII. Future Research	 57
 VIII. References	 59
 IX. Appendices	 60
1. Appendix A: Internship Importance	60
2. Appendix B: Input Parameters	61
3. Appendix C: Solution Convergence	63
4. Appendix D: Numerical Data	65
5. Appendix E: Animation 1	66
6. Appendix F: Animation 2	70
7. Appendix G: Animation 3	71
8. Appendix H: Animation 4	72

LIST OF FIGURES

Figure 1. Comparison of F/A-18E with F/A-18C	6
Figure 2. Top-down view of F/A-18E showing location of LEX vents	7
Figure 3. Flowchart detailing entire CFD process.	14
Figure 4. Close up of aircraft nose showing viscous layer of grid.	18
Figure 5. Three major steps of surface grid generation.	19
Figure 6. Final surface grid generation of entire aircraft.	26
Figure 7. Photograph of trailing edge flap/launcher junction.	27
Figure 8. Photographs of LEX vent.	29
Figure 9. Image of engine inlet showing location of negative volume cells.	30
Figure 10. Photograph of tufted model in wind tunnel at 0° angle-of-attack	32
Figure 11. Photograph of tufted model in wind tunnel at 16.08° angle-of-attack	32
Figure 12. Wind tunnel data of C_L versus α	33
Figure 13. Wind tunnel data of rolling moment versus α showing effect of sideslip on wing drop.	34
Figure 14. Wind tunnel β sweep of aircraft showing C_l' versus β .	35
Figure 15. Wind tunnel data showing effect of different LEF positions.	36
Figure 16. Lift curve of entire aircraft showing presence of wing drop.	42
Figure 17. Lift curve of outer wing.	43
Figure 18. Lift curve of inner wing.	43
Figure 19. Component lift buildup for vent-closed configuration.	44
Figure 20. Component lift buildup for vent-open configuration.	45
Figure 21. Difference in aircraft rolling moment between the two configurations	46
Figure 22. Surface pressure distribution on aircraft at 12° angle-of-attack	48
Figure 23. Surface pressure distribution on aircraft at 16° angle-of-attack.	49
Figure 24. Surface Mach number distribution on aircraft at 12° angle-of-attack.	50
Figure 25. Surface Mach number distribution on aircraft at 16° angle-of-attack.	51
Figure 26. Off-body pressure distribution at 12° angle-of-attack.	52
Figure 27. Off-body pressure distribution showing difference in vortex characteristics.	53
Figure 28. Off-body pressure distribution at 15° angle-of-attack.	54
Figure 29. Off-body pressure distribution at 16° angle-of-attack.	55
Figure C1. Residual plot over time.	64
Figure C2. C_L variance over time.	64
Figure C3. C_M variance over time.	64

LIST OF SYMBOLS

C_D	Drag coefficient
C_L	Lift coefficient
C_l	Rolling moment coefficient
E_t	Total energy per unit volume
f	Fuel to air ratio
M	Mach number
p	Pressure
q	Heat transfer
Re	Reynolds number
t	Time
u	Velocity component in X direction
v	Velocity component in Y direction
w	Velocity component in Z direction
α	Angle-of-attack of aircraft
β	Sideslip angle of aircraft
μ	Absolute viscosity
ρ	Density
τ	Viscous stress tensor

I. BACKGROUND

The purpose of this project was to use computational fluid dynamics to study wing drop on the F/A-18E/F in Powered Approach (PA) configuration. This involved a close study of the airflow characteristics over the aircraft, especially in the areas surrounding the LEX vents in hopes of understanding why the wing drop phenomenon occurred and the mechanics of how it was solved.

1. LEX VENT HISTORY

The F/A-18E/F was designed to improve upon the performance characteristics of the older F/A-18C/D aircraft. Improvements were desired in range, payload, growth potential, carrier bring-back, and survivability. To accomplish this, the initial design of the F/A-18E/F increased the dry weight of the aircraft and the wing area by twenty-five percent. The other control surfaces were then altered to accommodate the increase in

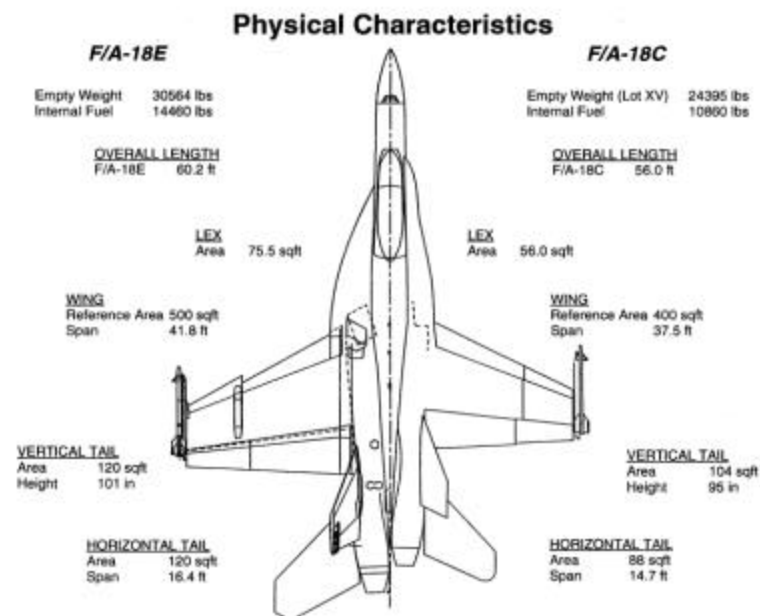


Figure 1 Comparison of F/A-18E with F/A-18C.

weight and wing area.

Preliminary tests revealed a significant degradation in the lift generated on the wings and the existing Leading Edge Extensions (LEX), leading to an increase of the size of the LEX and an alteration of its shape. The newly designed LEX started farther back on the fuselage, and instead of having a S-shape, the span of the LEX was increased and was changed to a parabolic shape. These changes provided the increase in lift needed to regain the desired performance. The differences between the LEX on the F/A-18C and F/A-18E can be seen above in Figure 1.

During this LEX redesign, the increased span of the LEX decreased the Leading Edge Flap (LEF) span, and significantly affected the aerodynamics surrounding the flap deployment. A vent in the LEX adjacent to the Leading Edge Flaps was created to compensate. Figure 2 depicts a top-down view of the aircraft showing the location of the

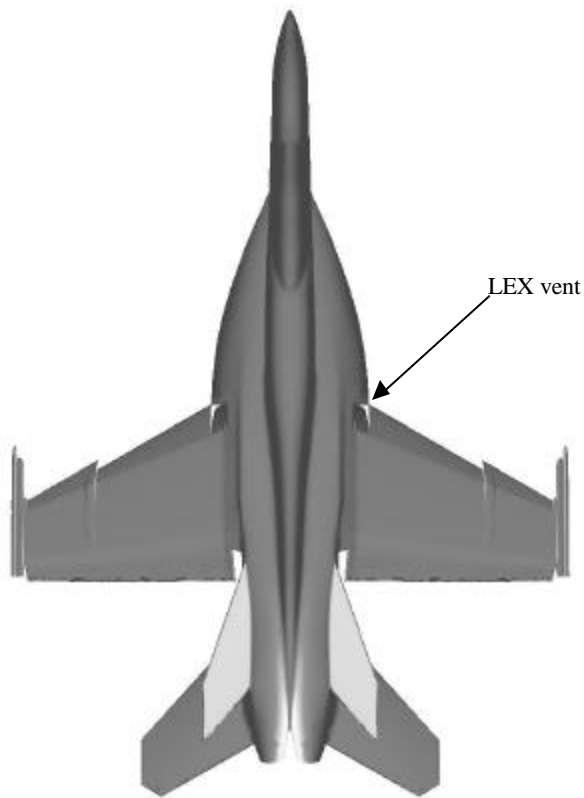


Figure 2 Top-down view of F/A-18E showing location of LEX vents.

vent. The vent created an effective extension of the LEF into the LEX.

Wind tunnel tests of the LEX vent configuration revealed several additional aerodynamic benefits:¹

- ◊ Increased nose-down pitching moment (providing high angle-of-attack controllability)
- ◊ Increased lateral-directional stability (enhancing departure resistance and lateral-directional flying qualities)
- ◊ Increased maximum lift (improving instantaneous turn performance)
- ◊ Decreased vertical tail buffet (alleviating fatigue)
- ◊ Increased lift in PA configuration (decreasing approach speed)

Due to the cruise drag of a fixed vent, the vent was actuated to open at high angles of attack (above 20°) to provide the above aerodynamic benefits, and close at low angles of attack (less than 12°) to reduce the drag.¹ Vent operation was automatic, with only two positions: fully-open and fully-closed. When open, the vent flap was deflected to 33.5° leading edge down.

In the Power Approach (PA) configuration, the vent was automatically commanded to the open position, regardless of angle-of-attack. The PA configuration is defined as the landing gear extended, the trailing edge flaps fully deflected to 40°, and the leading edge flaps programmed on an angle-of-attack schedule. This configuration is used for field and shipboard landings and shipboard (catapulted) takeoffs. PA configuration is a relatively low speed configuration with a Mach number of 0.17.

During initial flight tests of the aircraft in February 1996, a phenomenon known as “wing drop” was discovered when the aircraft was in PA configuration.¹ Flight tests in this configuration revealed the wing drop would occur when the aircraft’s angle-of-attack approached 12E. Wing drop was officially defined as “an abrupt, uncommanded, roll acceleration.” In other words, wing drop is an asymmetric loss of lift from one wing,

resulting in a momentary degradation in control of the aircraft. Later flight tests showed⁹ that by closing the LEX vent, the wing drop disappeared. The original cause of the problem and the mechanics of how it was solved were never fully understood. Due to budget and time constraints, however, the program moved on, and a full study of this phenomenon was never undertaken.

At that point, the LEX vents were disabled electronically for the PA configuration and retained in the Up and Away (U/A) configuration. Subsequent U/A testing discovered the vents delivered none of the promised benefits. They were consequently deleted from the design of the production aircraft, resulting in a hefty cost and weight savings.¹

This project was initiated in spring of 1999 by the Naval Air Systems Command (NAVAIR) to understand the origin of the problem to determine if technical lessons could be gleaned so that a similar problem could be avoided in future designs.

2. CFD BACKGROUND

The study of PA wing drop requires the use of computational fluid dynamics, or CFD. CFD is a relatively new and growing field in aeronautical engineering today because of its basis in high speed computers. As there were no computers until just recently that could handle solving fluid dynamic problems of any complexity, it has taken many years for CFD to come of age and reach its current status. Its history is primarily composed of advances in three domains: “aerodynamic (fluid-dynamic) theory, applied mathematics, and computers.”²

The equations that were developed over the past two centuries to model and describe fluid flows are very complex integral or nonlinear partial differential equations and are thus extremely difficult to solve. In fact, no general analytical solution exists for these governing equations. All fluid dynamicists could do was obtain analytical solutions

for simplified or restricted forms of these equations. Computational fluid dynamics offers a better alternative than trying to restrict or simplify the equations. CFD is “the art of replacing the governing nonlinear partial differential equations with numbers, and advancing these numbers in space and/or time to obtain a final numerical description of the complete flow field of interest.”³ Although CFD gives lists of numerical data rather than a compact solution, it allows the researcher to solve the governing flow field equations exactly, without having to make any restrictions or simplifications of the governing equations.

The first computational fluid dynamics work was not really started until the late 1960's and early 1970's, awaiting the necessary computer speed and storage capacity. Since the 1980's and 1990's, computer processing speed and storage capacity grew so extensively that computational aerodynamics could become a viable research tool. As this method started becoming accessible, researchers began to use the CFD methods more frequently for all types of problems. Before CFD, the only way to obtain flow data was from wind tunnel tests. Wind tunnel tests are very expensive and not always accurate, because they are extremely difficult to run at the same Reynolds number as an in-flight aircraft. The Reynolds number is a non-dimensional quantity that is “physically a measure of the ratio of inertia forces to viscous forces in a flow and is one of the most powerful parameters in fluid dynamics.”⁴ The Reynolds number affects the dynamic behavior of viscous flows and provides dynamic similarity between flow fields of the same Reynolds number. Since the Reynolds number is very important in the pressure distributions of flow separations and transonic flows, only very expensive wind tunnel tests can be relied upon in these instances. Thus, CFD has become extremely important as an independent research tool that can provide better insight into these types of complex flows. CFD is now being used in every major aerospace firm, and is extensively used for military applications by organizations like NAVAIR.

High Reynolds number flows, which are common in flight, exhibit two distinct

regions surrounding an aircraft in its flight: A boundary layer adjacent to the surface where viscous effects are confined, and a region outside the boundary layer where viscous effects are negligible.

This CFD study used the USM3D flow solver developed by the NASA Langley Research Center (LaRC). This solver solves two major sets of governing equations to account for flows inside and outside of the boundary layer. Both sets of these equations are derived from the universal laws of conservation. These laws represent the conservation of mass, momentum, and energy. When applied to compressible, viscous fluid flows, these conservation laws yield the continuity, momentum, and energy equations, respectively, which are commonly referred to as the Navier-Stokes equations. Written in Cartesian form, without body forces or external heat addition, these equations are shown below.

$$\begin{aligned}
 \frac{\partial \mathbf{U}}{\partial t} + \frac{\partial \mathbf{E}}{\partial x} + \frac{\partial \mathbf{F}}{\partial y} + \frac{\partial \mathbf{G}}{\partial z} &= 0 \\
 \mathbf{U} &= \begin{bmatrix} \mathbf{r} \\ \mathbf{r}u \\ \mathbf{r}v \\ \mathbf{r}w \\ E_t \end{bmatrix} \\
 \mathbf{E} &= \begin{bmatrix} \mathbf{r}u \\ \mathbf{r}u^2 + p - \mathbf{t}_{xx} \\ \mathbf{r}uv - \mathbf{t}_{xy} \\ \mathbf{r}uw - \mathbf{t}_{xz} \\ (E_t + p)u - u\mathbf{t}_{xx} - v\mathbf{t}_{xy} - w\mathbf{t}_{xz} + q_x \end{bmatrix} \\
 \mathbf{F} &= \begin{bmatrix} \mathbf{r}v \\ \mathbf{r}uv - \mathbf{t}_{xy} \\ \mathbf{r}v^2 + p - \mathbf{t}_{yy} \\ \mathbf{r}vw - \mathbf{t}_{yz} \\ (E_t + p)v - u\mathbf{t}_{xy} - v\mathbf{t}_{yy} - w\mathbf{t}_{yz} + q_y \end{bmatrix} \\
 \mathbf{G} &= \begin{bmatrix} \mathbf{r}w \\ \mathbf{r}uw - \mathbf{t}_{xz} \\ \mathbf{r}vw - \mathbf{t}_{yz} \\ \mathbf{r}w^2 + p - \mathbf{t}_{zz} \\ (E_t + p)w - u\mathbf{t}_{xz} - v\mathbf{t}_{yz} - w\mathbf{t}_{zz} + q_z \end{bmatrix}
 \end{aligned} \tag{1}$$

The first row in the above vectors corresponds to the continuity equation. The next three rows correspond to the three dimensional momentum equation, and the last row corresponds to the energy equation.

Once outside the viscous boundary layer, however, the viscous effects of the fluid are ignored, and the solution is solved under the assumption of inviscid flow. Thus, the governing equations outside the boundary layer are much simpler and are entitled Euler's equations for inviscid flows. Neglecting all viscous effects ($\tau=0$), the governing equations take the following form:

$$\frac{\partial \mathbf{U}}{\partial t} + \frac{\partial \mathbf{E}}{\partial x} + \frac{\partial \mathbf{F}}{\partial y} + \frac{\partial \mathbf{G}}{\partial z} = 0$$

$$\mathbf{U} = \begin{bmatrix} \mathbf{r} \\ \mathbf{ru} \\ \mathbf{rv} \\ \mathbf{rw} \\ E_t \end{bmatrix}$$

$$\mathbf{E} = \begin{bmatrix} \mathbf{ru} \\ \mathbf{ru}^2 + p \\ \mathbf{ruv} \\ \mathbf{ruw} \\ (E_t + p)u + q_x \end{bmatrix} \quad (2)$$

$$\mathbf{F} = \begin{bmatrix} \mathbf{rv} \\ \mathbf{ruv} \\ \mathbf{rv}^2 + p \\ \mathbf{rvw} - \mathbf{t} \\ (E_t + p)v + q_y \end{bmatrix}$$

$$\mathbf{G} = \begin{bmatrix} \mathbf{rw} \\ \mathbf{ruw} \\ \mathbf{rvw} \\ \mathbf{rw}^2 + p \\ (E_t + p)w + q_z \end{bmatrix}$$

The USM3D flow solver is a cell-centered, finite volume flow solver. In this project, it was used to solve an unstructured grid. This type of grid was used due to the highly complex aircraft geometry. The unstructured grid allows a complex geometry to be modeled without driving the cell count too high. If a structured grid had been implemented, the total number of cells needed to model the aircraft would have been too high, thus requiring an excessive amount of CPU time to solve the problem.

In solving the unstructured grid, the flow solver can implement both explicit and implicit finite difference schemes. These techniques transform the governing partial differential equations into a system of algebraic equations for the flow parameters. USM3D uses a Runge-Kutta method for explicit calculations and a Gauss-Seidel method for implicit calculations of the system of algebraic equations. Because of the availability of computer memory, the implicit method was used in this project. This allowed for the flow solver to have a better chance of achieving convergence as well as taking much less time than the explicit method.

Detailed background information on all of the underlying algorithms in the flow solver can be found by referring to LaRC's extensive bibliography.⁵

II. PROCEDURE

The computational study of the F/A-18E Super Hornet involved a multi-step, detailed process using industry standard flow solvers developed by the NASA Langley Research Center. The study used the Tetrahedral Unstructured Software System (TetrUSS) suite composed of four interdependent modules: GridTool, VGRID, USM3D, and VigPlot. These programs were created by NASA for government use and were specifically designed to allow CFD calculations for the “non-expert user.”⁶ They were all based on the unstructured grid modeling technique. An overview of the TetrUSS suite may be found at the LaRC website.⁷

The sections below outline the function of each of the TetrUSS modules, for the organization of the modules dictated the process by which the study was performed. Figure 3 depicts the flow through the four TetrUSS modules.

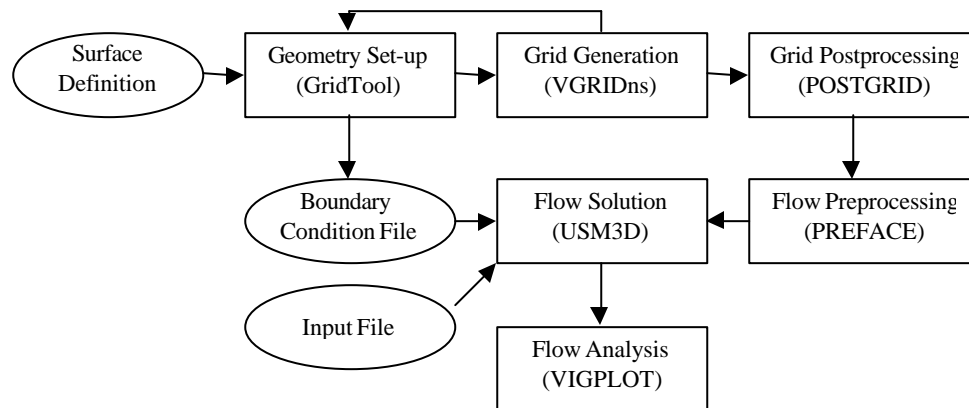


Figure 3 Flowchart detailing entire CFD process.

1. SURFACE CONSTRUCTION⁶

GridTool was the first computer program used in the computational study. This module of the TetrUSS package was the most important part and played the biggest role in the entire CFD process. GridTool was used to define the shape of the aircraft and prepare it for the grid that was later generated. GridTool also defined the grid density and distribution.

The first step in using GridTool was to obtain a high-definition geometry that modeled the aircraft as accurately as possible. For this study, considerable communication with Boeing was required to obtain a “watertight” model, or one that was continuous with no gaps or holes, that represented all geometric aspects of the aircraft as accurately as possible. Since current flow solvers cannot yet read the surfaces of the aircraft straight from a Computer-Aided-Design (CAD) format, the surface geometry was first traced out and defined in a format that the flow solver could use. This process involved outlining the surfaces with points and curves to model the shapes and curves of the aircraft as accurately as possible.

Next, the outlined geometry was broken into patches constructed from these curves.⁶ These patches constructed the starting point for the volume grid, and modeled the exact shape of the aircraft. The patches also had to meet specific criteria in order for the grid to generate properly. All of the patches had to be three or four-sided and as regular as possible in shape. High aspect ratio patches or patches with extremely acute angles were also avoided as they rendered irregular triangles when the grid generation began. Additionally, the patches had to be as planar as possible. Since the curve and shape of the patch was what the flow solver understood to be the surface of the aircraft, the patches had to accurately represent the surface geometry. The surface grid generator used cubic splines to match curved surfaces and so did not model the sharp surface curves perfectly, unless the highly curved areas of the surface were broken into appropriate patches. Patching was the most time consuming but yet the most important

part of the entire CFD process and was done entirely with the GridTool software.

Once the aircraft was modeled entirely with “watertight” curves and patches, background sources were added to the model. These sources determined the density and size of the grid to be generated. The sources could either be point sources or linear sources and were at places from which the grid begins to generate. The sources could be placed either inside or outside the aircraft body. Complex geometric areas and those areas with large flow gradients, such as the area surrounding the slotted flap, needed to have a smaller and denser grid than those areas such as the middle of the wing where shallow flow gradients could be expected. Grid density determined both the numerical convergence properties and the accuracy of the flow solution.

However, computational cost grew exponentially with total node count, so a compromise had to be reached. Thus, the grid was no more dense than necessary to achieve convergence in the areas where the large gradients occur. Placing the sources involved a trial and error process, since the particulars of the flow were not known until a solution was attempted. Since placing these sources is an art, experts in CFD at NAVAIR helped throughout this process. They provided insight into what has and what has not worked in the past regarding aircraft geometries. In this study, some of the areas on the aircraft where this dense grid was required were the area surrounding the LEX vent, the area surrounding the snag of the wing, the slotted flap, and the wing tip.

Once the aircraft was fully modeled and the sources were placed, a box was created containing the aircraft and the area surrounding it. This box defined how big the entire volume grid would be and must be large enough to include all flows affected by the presence of the aircraft. Previous CFD work suggested a box having a length six times the length of the aircraft, and a height and width three times the length of the aircraft.

One other part of the surface construction phase was the definition of the boundary conditions for various surfaces. This was a very critical step since this CFD problem was a boundary-value problem. This step involved assigning a certain boundary

condition to each individual patch that matched the type of flow at that location. Some of the boundary conditions that were used on the aircraft itself include viscous, inviscid, engine inlet, and engine exhaust. Other boundary conditions used in this problem were flow-through and reflection plane. The flow-through condition was used on all of the walls of the surrounding box except for the wall the aircraft lies on. This condition marks the boundaries of the flow solution and acts as a transparent surface allowing all flow to pass through. The reflection plane condition was used on the wall of the box that contains the aircraft body. This condition acts just as a reflection plane assuming a symmetric aircraft.

2. GRID GENERATION⁸

The next step of the CFD process was to generate a surface grid on each patch of the model. This was done using the VGRID software and involved loading the geometry with the sources into the VGRID database and generating a surface mesh on each patch based on the defined sources. Each patch was then examined to evaluate the mesh generated, and to make sure that the mesh was good and that there were no highly irregular triangles. A good mesh was defined as one that did not contain any skewed or distorted triangles. When bad meshes were found in this process, there were three things that were done. One method included rotating the patch so that the grid generation began on a different side. The surface grid generation algorithm started from one side of the patch and worked outward so the final mesh was directly related to from which side of the patch the mesh was started. If this did not correct the problem, another method involved altering the actual shape of the patch. This method involved going back into GridTool, and either splitting the patch or rearranging the patch geometry to yield a “better” patch. The third method of correction involved changing the nearby source size and intensity in order to affect how the mesh is generated. This method was not used very often, however, as most problems were due to a bad patch shape or orientation.

After each patch was grid meshed satisfactorily, the model went back into GridTool, and stretching was applied. The stretching process involved stretching the grid in various places where no large gradients were present to further reduce cell count. This process included the spanwise stretching of the wing and flaps. During the stretching process, the viscous boundary layer was also defined, which told the grid generation software where viscous flows were present, and how large to make the viscous portion of the grid. The viscous grid generation algorithm used an advancing layer method to generate the viscous layer, based on the following properties: the initial thickness of the layers, the number of layers, and the thickness of each following layer. A Blasius calculation for a flat plate determined the thickness of the boundary layer, and the number obtained was then used to determine the thickness of the initial layer and the number of layers needed. Once the viscous grid was generated, the geometry was taken back into VGRID, and the surface mesh was regenerated; this time accounting for the stretching and viscous effects. In Figure 4, a close-up of the nose of the F/A-18E depicts this viscous layer and how it differs from the inviscid portion of the grid. The grid generation process until this point can be summarized by Figure 5, which shows the major steps necessary to create a surface mesh.

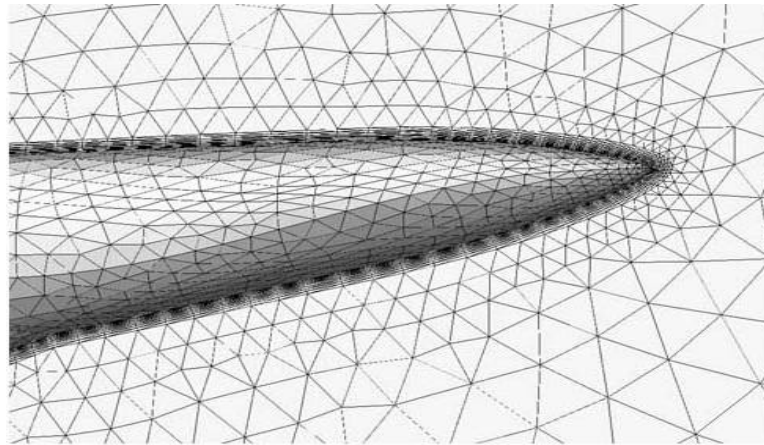


Figure 4 Close-up of aircraft nose showing viscous layer of grid.

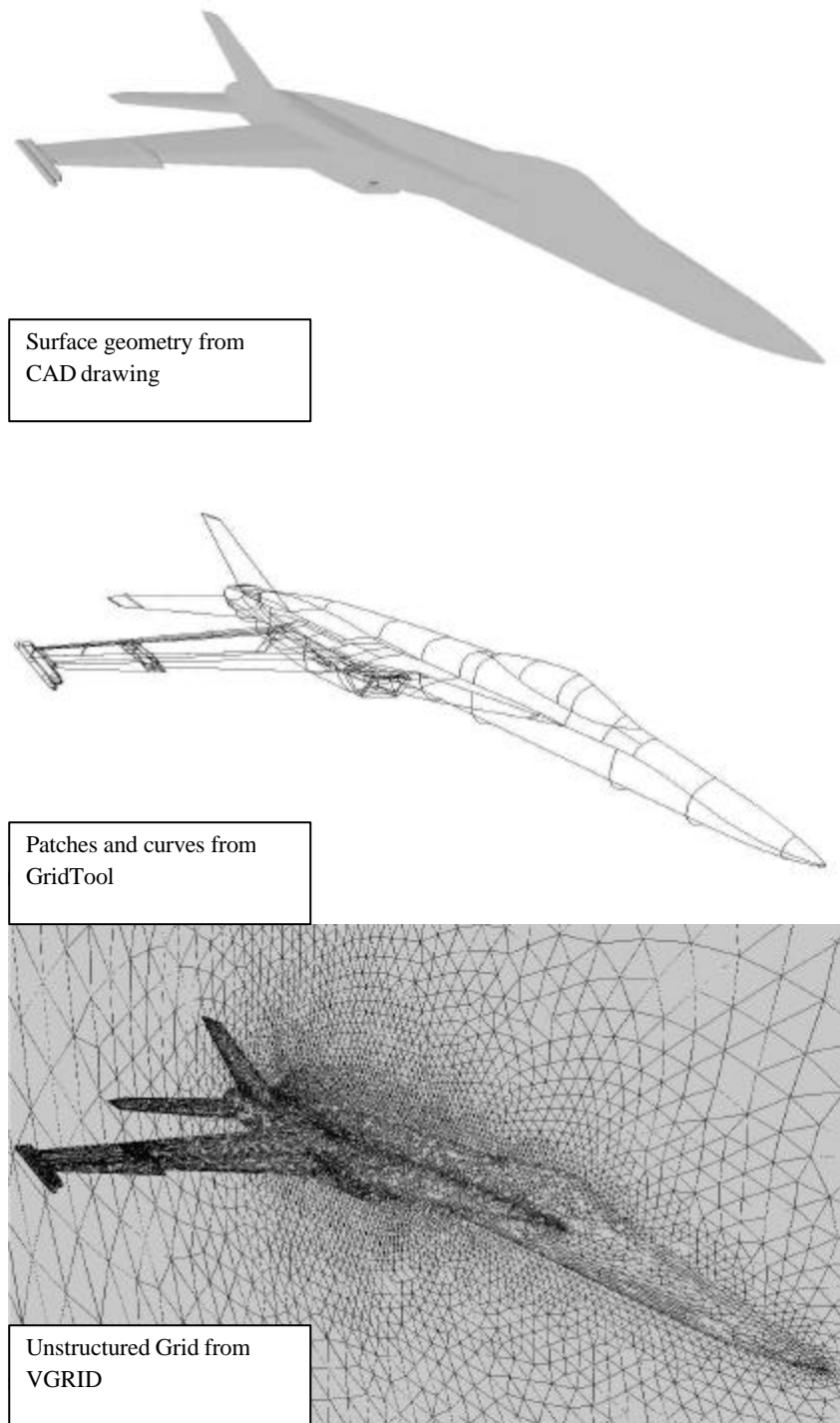


Figure 5 Three major steps of grid generation.

The generation process continued outward and created a volume grid after the surface mesh was generated with the VGRID software. Before this process began, however, the program computed all the unit vectors normal to the surface for the advancing layers. These vectors determined how the grid would grow. They defined the direction of layer growth for each patch. If these vectors were considered bad, or invisible, then a mesh would not be generated in this location. A vector was considered invisible when it pointed into another surface, going against the vector pointing out from the penetrated surface. When this problem occurred, the grid generation was aborted and the problem was addressed.

Problems occurred here from poor background source selection or highly concave geometries. Once these problems were fixed in GridTool, the entire surface and volume generation process was redone in order to reflect the changes made to the model.

When a final volume grid was generated, a small utility program, POSTGRID, analyzed the entire grid and identified trouble spots where the flow solver would likely run into problems. Portions of the grid could then be cut away and rebuilt in the problem areas to try to obtain a smoother mesh. Once the entire process was completed, the volume grid was taken back into GridTool again so that the surface front could be projected onto the surface geometry. This step accounted for any curvature that was present in the patches that the splines failed to match precisely.

3. FLOW SOLUTION AND ANALYSIS⁹

After the volume grid was projected back onto the aircraft surface, the grid was solved using the flow solver USM3D. In order to run properly, the flow solver required the grid file as well as an input file listing all the initial conditions governing the problem, such as freestream pressure, temperature, and Mach number. The input file also included engine specific data used by the flow solver to model the engine exhaust and the mass flow rate into the inlet. A table listing all of the input variables as well as a sample input

file can be found in Appendix B. The flow solver was then run at various angles of attack to get a range of solutions. The output obtained included data tables listing the airflow characteristic distributions over the entire aircraft. This data was displayed visually using the computer program entitled VigPlot. Once this was done for one stabilator position, a different stabilator position was used in the initial geometry and the entire process was repeated to get a full sensitivity analysis.

III. TEST EQUIPMENT

The entire grid generation process was done using Silicon Graphics (SGI) machines in the USNA (CADIG) facility. The flow solver, USM3D, was run on two different computer systems. Some runs were done using the USNA CADIG facility, and some were done using a CRAY supercomputer at the Naval Oceanographic Office (NAVO) facility in Mississippi. These special computers were used because of the large computational time needed to achieve convergence on a solution for these sizes of grids. For a problem such as this with over a million grid points, approximately 20 hours of CPU time was needed to achieve a solution.

IV. MODEL GENERATION

1. INITIAL GEOMETRY SELECTION

For the solution to be a good representation of the actual airflow over the F/A-18E, the geometry used must represent the aircraft in PA configuration as closely as possible. Thus, the geometry must have a highly detailed wing, especially in the area surrounding the LEX vent. A model must also be obtained of the aircraft with the LEX vent closed in order to have a clean configuration solution for comparison. These geometries must also contain the wing-tip missile and launcher, as the aircraft is always flown with these components.

In order to begin grid generation, a 'watertight' (having no gaps or holes) high definition surface geometry of the F/A-18E in PA configuration was requested from Boeing, the airplane's manufacturer. Boeing sent a volume geometry that was supposed to contain the needed surfaces. Since no specific surface coordinates were sent, however, the exact surface could not be accurately obtained from this volume geometry. A more specific model was then requested from Boeing, and two other geometries were sent. Boeing provided a full aircraft in PA configuration and a high definition wing in PA

configuration. Instructions were also sent stating that the full aircraft had an old-style wing and thus the old style wing must be replaced by the high definition wing. Upon completion, it was found that the aircraft fuselage had many large gaps and holes. After consulting with Boeing, it was determined that this fuselage model was indeed a rough outline of the fuselage and had never been completed due to project cancellations. In response, Boeing sent the I-J-K coordinates necessary to obtain the specific surface geometry from the first volume geometry sent previously. A careful analysis found that the wakes had been included with this surface making it difficult to determine where the aircraft surface ended and the wakes began. Also, the wing box and trailing edge flaps were roughly modeled and did not represent the actual F/A-18 wing to the accuracy needed for this project. This surface model was also found to be a much smaller, unknown scale model compared with the other geometries sent. Another surface geometry, previously used in another CFD project, was then obtained from an engineer at NAVAIR. This geometry was of the aircraft in a proper scale and location but not in the PA configuration.

At this point, no complete model existed, but the following existed in inventory: a high definition wing in high lift configuration in a 1:1 scale, a full PA configuration aircraft with an inaccurate wing in an unknown scale, a full aircraft not in PA configuration but in a 1:1 scale, and a PA configuration fuselage with many gaps and holes in a 1:1 scale.

Three options became available: (1) Mate the high definition wing to the 1:1 scale PA configuration surface, and attempt to fill in the many gaps that were present. Many approximations would have been necessary in order to fill in these gaps and make the geometry 'watertight'. (2) Mate the high definition wing to the full PA configuration in the unknown scale. Because this scale was unknown, it would have been difficult to re-scale it accurately and then translate it to match up with the high definition wing without many approximations. (3) Mate the high definition wing to the 1:1 scale aircraft

not in PA configuration. This option would involve switching out the wings and the horizontal stabilizers. Some approximations would be needed to match up the high definition wing with the non-PA fuselage. This option seemed to involve the least amount of approximations, which would result in the most accurate final model. Thus, the third option was chosen and the initial surface geometry was created.

2. MODEL CHALLENGES

During the construction of the grid, certain areas arose in the geometry that had to be simplified in order to allow the grid generation to take place. In general, these areas were usually areas where the geometry came to a singularity, or where very sharp angles were present.

The junction between the trailing edge flap and the aileron was one problem area. At this junction, there was a scissor-like geometry where the leading edge of the flap and the aileron came together to a singular point at a very acute angle. A grid could not be generated in this type of area so the geometry had to be adjusted to achieve a good meshing of the grid. This adjustment involved putting a small wedge into the junction so that the flap and aileron were blended.

Another problem area was the junction between the trailing edge flap and the fuselage. The final geometry obtained did not properly model this junction according to the actual shape of the aircraft. Instead, a very large gap, (approximately six-inch) was present between the flap and fuselage where none actually exists. This was due to a poor representation of the area by the surface geometry received from Boeing. In order to model this area with something close to the actual geometry rather than a gaping hole, the flap shroud and the cove were extended to connect with the fuselage. The flap itself was left alone, and an unrepresentative gap is evident in the planform pictures.

One of the more challenging details of the PA configuration was the cove in the wing into which the flap retracts when raised. From previous CFD calculations, no

significant flow gradients have been found spanwise along the cove.¹⁰ Furthermore, the same studies have indicated that external flows are not affected by the cove geometry. Thus, in order to cut down on grid size and complexity, the cove was simplified significantly and its size was cut down.

One concern with CFD models is the area surrounding the engine, including the inlet, exhaust, and inside of the engine cowl. Since the purpose of this CFD investigation was not to model the airflow within the engine, this area was greatly simplified; to maintain fidelity, however, the engine could not just be modeled as a hole with nothing there. Given engine operating data, the flow solver accounted for the mass flow through the engine, without having to model the interior of the engine. The engine inlet was modeled as flow through, similar to the actual engine inlet. The grid was cut off just inside the inlet to cut down on the size and was started again at the nozzle exit plane. Actual engine exhaust characteristics were then assigned to the exhaust flow, and USM3D performed the mass flow balancing. These characteristics can be found in Appendix B.

After these geometry selections were made and implemented on the aircraft model, a final surface mesh was generated. The mesh can be seen in Figure 6 on the following page. The next step was to build outward from this grid to generate the volume grid. However, many problem areas arose when this was attempted.

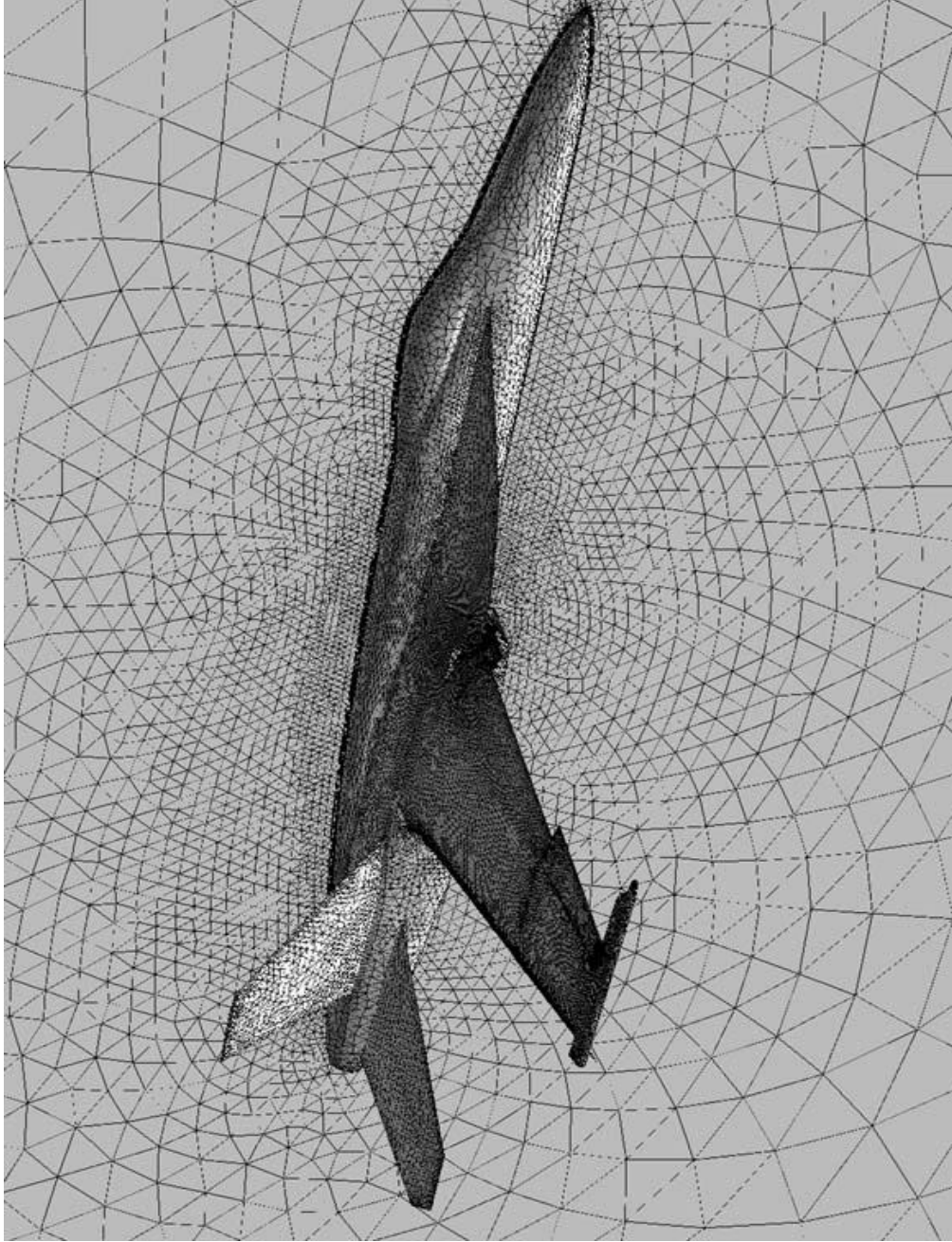


Figure 6 Final surface grid generation of aircraft.

3. PROBLEM AREAS

One of these problem areas was at the junction of the aileron shroud, the trailing edge of the wingtip, and the rear of the launcher. The geometry available left a small gap between the shroud and the launcher where a small piece of the trailing edge of the wingtip was exposed. Although this is the actual geometry of the aircraft, a grid could not be generated in this area due to the many sharp angles and thin gaps. Because of this type of geometry, VGRID faulted when trying to compute the surface vectors. In order to alleviate this problem, the size of this gap was increased, and its shape was slightly altered. This added geometry should not affect the overall airflow properties over the wing or have anything to do with the wing drop phenomenon itself. Along with these geometric simplifications, the source located in that area was made smaller and its influence was increased. These changes together erased the invisible vector and solved the problem in this area. This problem area can be seen in Figure 7, which is a photograph of the actual trailing edge flap/launcher junction of the F/A-18E. The aforementioned gap is visible in the center of the photograph next to the orange-colored wingtip.



Figure 7 Photograph of trailing edge flap/launcher junction.

One other area that required a simplification of the geometry was the entire LEX vent area itself. The complex geometry present in the area surrounding the LEX vent caused many problems in the volume grid construction. Many invisible surface vectors were computed here, precluding successful grid generation. This geometry had to be treated carefully, however, since this vent was the focus of the entire project. Significant simplification would risk either corrupting the very phenomenon under study, or invalidating the study altogether. The geometry provided showed an abrupt end of the leading edge flap and a wedge-shaped gap between the vent and the end of the leading edge flap. This wedge-shaped gap caused many problems in the viscous grid generation part of the grid generation process. Thus, the gap had to be modified in such a way to generate a viscous layer of cells in the gap, but not lose the general shape of the area so as not to unrealistically alter the airflow. This problem was solved by altering the gap's shape to more of a rectangular shape, instead of coming down to a singular point. This step allowed for cell formation, while still keeping the general shape of the actual geometry. This geometry is displayed in Figures 8a and 8b. Since the LEX vents have now been disabled on the flight test aircraft, no photograph with the vent open could be obtained. These two views show the shape and orientation of the LEX vent, however, in its stowed configuration. The above problems occurred during the surface grid generation.

Two more major problems arose after the viscous portion of the volume grid was completed. Once the viscous layers were generated, the computer program analyzed the layers to make sure the grid was still usable. This involved looking for cells that have a negative volume, where advancing layers opposite each other have become entangled and have distorted the cells present. This occurred in two areas of the grid.

One of these negative cell problem areas was the slot. All along the length of the slot, negative cells were found, with a significant portion of them near the outer wing where the cove is smaller. Though many adjustments of source size and intensity were



Figure 8a Side view of LEX vent.



Figure 8b Front view of LEX vent.

made in the slot, the negative cells remained. A reduction in the number of negative cells occurred with an increase in the number of cells in the slot; however the large increase in total cell count was not producing enough of a reduction in the number of negative cells.

The grid size was becoming too excessive to warrant the inclusion of the slot. Thus, the slot was eliminated from the geometry altogether. This caused a significant reduction in the cell count of the entire aircraft model. The validity of this substantial change will be discussed in the next section.

The other area containing the negative cells was the area surrounding the engine inlet and its junction with the aircraft fuselage. Surrounding the engine cowl and inlet is a gap between the lower surface of the wing, the fuselage, and the engine cowl itself. The negative cells formed in these areas. Figure 9 shows a wireframe image of the engine inlet with the negative cells shown. The size and intensity of the sources in this area were adjusted many times in trying to solve this problem. The number of cells were increased so much in this area that the entire aircraft grid count doubled. Even with this large increase in the grid density in this location, these negative cells were still present. Thus, the decision was made to solve the grid using the Euler inviscid calculations. For a viscous solution to be achieved, this inlet problem will have to be solved.

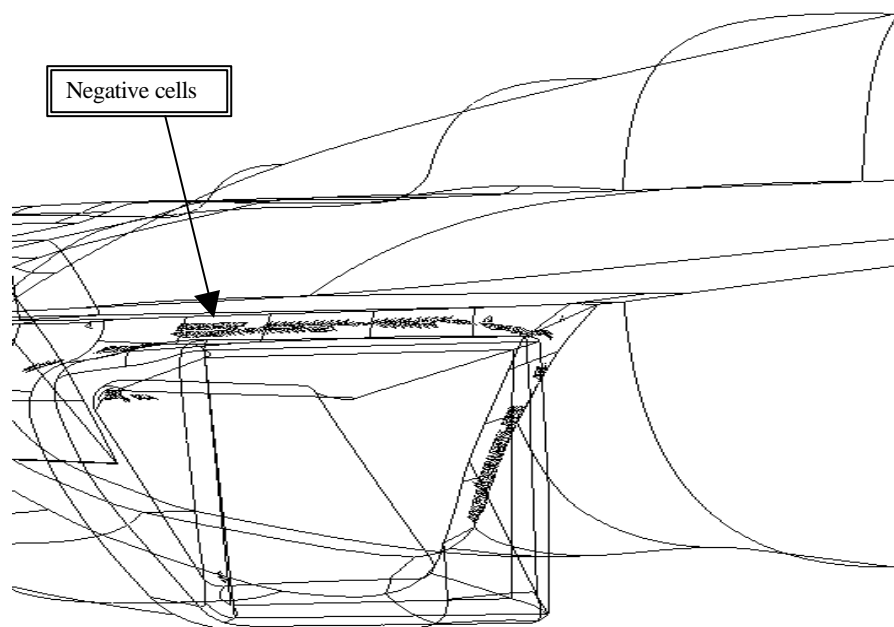


Figure 9 Image of engine inlet showing location of negative volume cells.

V. VALIDATION OF CFD MODEL

Validation of the computational results was heavily dependent on a wind tunnel study performed in August of 1999. Wind tunnel testing on the F/A-18E in the PA configuration with the LEX vent open and closed was conducted by Mr. Steve Cook, a NAVAIR researcher and doctoral candidate at the University of Maryland.¹¹ Results of this work will be published in 2001 and are included here with his gracious permission.

A ten-percent scale model was entered in NASA Langley's 12-foot low speed wind tunnel. The scope of those tests included a range of angles-of-attack, sideslip angles, various LEF deflections, and stabilator positions. The simplification of the computational model depended heavily on these data in order to ensure that the chosen simplifications did not invalidate the computational results. The qualitative and quantitative results summarized below substantiate the validity of several of the simplifying assumptions made for the CFD model.

1. WIND TUNNEL RESULTS¹¹

The August 1999 wind tunnel study provided both qualitative and quantitative results beneficial to the validation of the computational results.

First, luminescent tufts were employed as a means of flow visualization. Figures 10 and 11 depict the tufted-wing results at 0° and 16.08° angle-of-attack. In the first figure, the tufts on the main wing panels are all smoothly aligned with the freestream flow, indicating attached flow. In the second, at 16.08° angle-of-attack, the tufts are chaotically aligned, indicating that the flow over the outer two-thirds of the wing panels is separated. Furthermore, some significant asymmetric disturbances in the airflow over the wing can be seen. Given the gross macroscopic effect of such large separated regions, the computational study must be expected to also reflect these large separated regions.

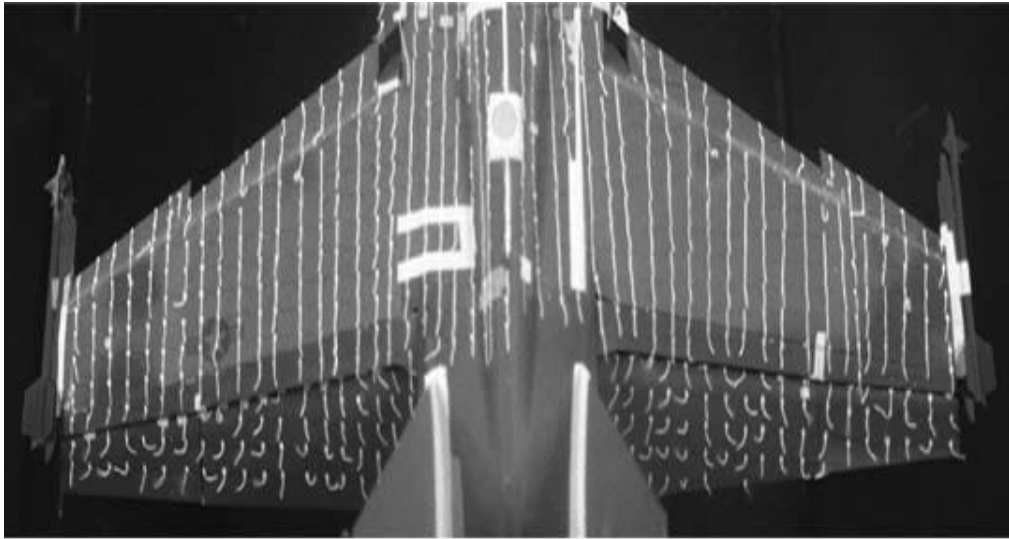


Figure 10 Photograph of tufted model in wind tunnel at 0° angle-of-attack.

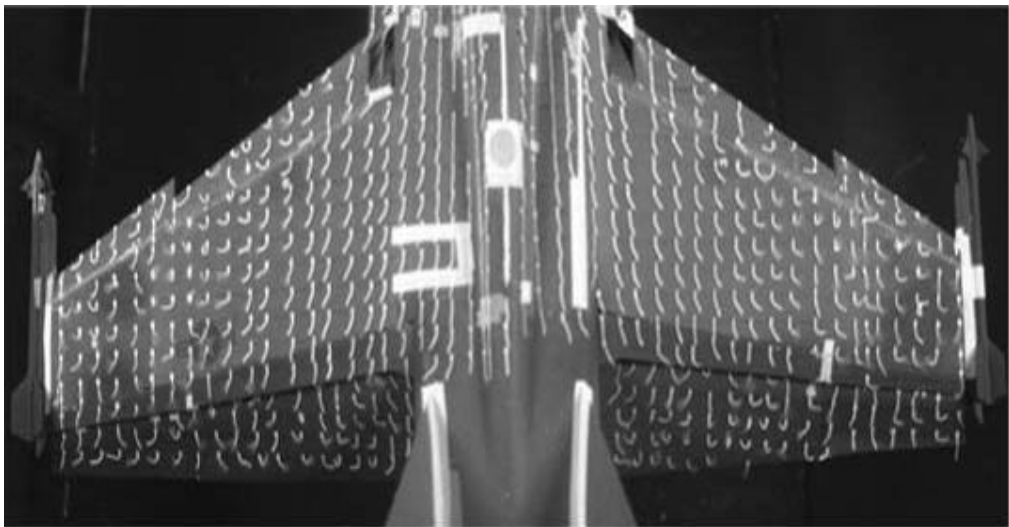


Figure 11 Photograph of tufted model in wind tunnel at 16.08° angle-of-attack.

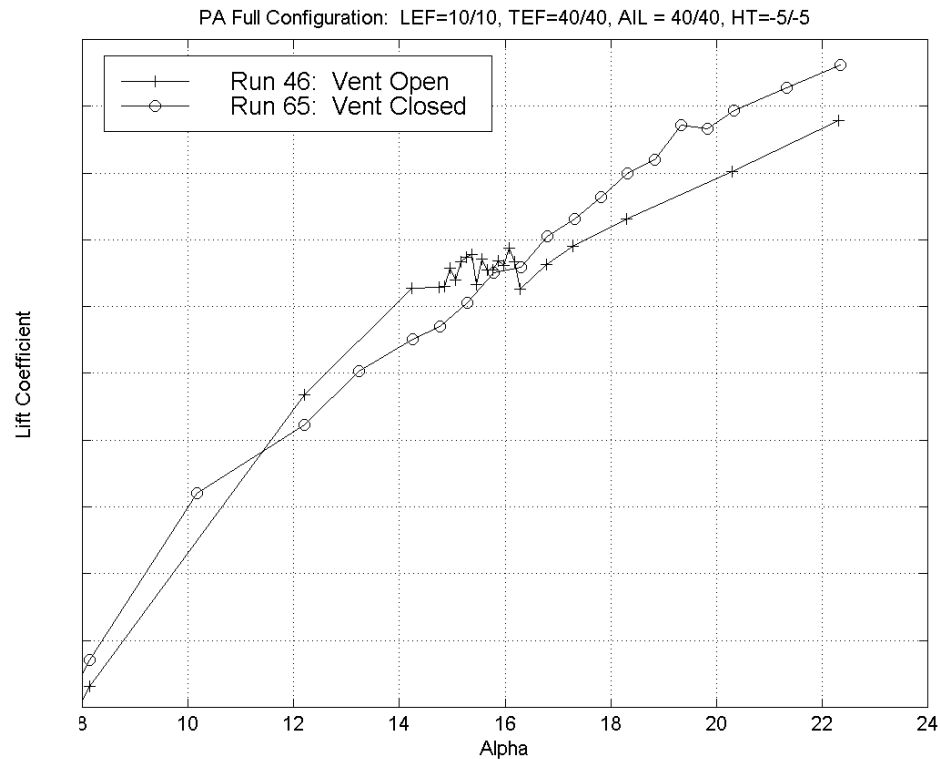


Figure 12 Wind tunnel data of C_L versus α .

Second, the wind tunnel study provided substantial quantitative data on the total lift variations with angle-of-attack. Figure 12 presents the lift coefficient plotted against the angle-of-attack for both the vent-open and vent-closed configurations. The lift values have been omitted awaiting formal release of the data by program officials. For the vent-closed configuration, the lift curve increases steadily with increasing α . The vent-open configuration, however, exhibits a precipitous drop in lift between 14° and 17° angle-of-attack.

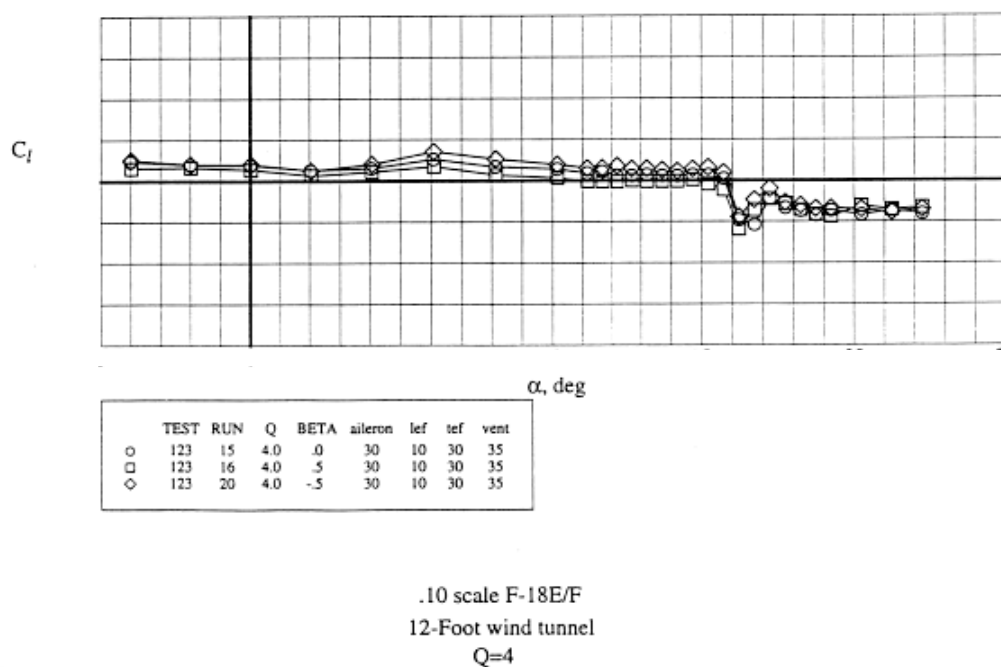


Figure 13 Wind tunnel data of rolling moment versus α showing effect of sideslip on wing drop.

The drop in the lift curve correlated with spikes in the rolling moment. The model was yawed about zero degrees sideslip to evaluate the effect of sideslip on the rolling moment. Figure 13 depicts the rolling moment at 0° , -0.5° , and $+0.5^\circ$ sideslip. Note that the strong asymmetry remains unchanged. Therefore, since the moment spike is insensitive to sideslip, an asymmetric rolling moment may exist in the presence of a symmetric freestream flow on a symmetric model (zero sideslip).

Although the wing drop is not dependent on sideslip, a β sweep provided further insight into the phenomenon. Figure 14 depicts the stability axis rolling moment versus sideslip angle. Whereas the vent-closed data exhibits a smooth linear variation of rolling moment, the vent-open data varies wildly between -1.5° and $+1.5^\circ$ sideslip. At large negative sideslips, the vent-open rolling moment is more positive than the vent-closed

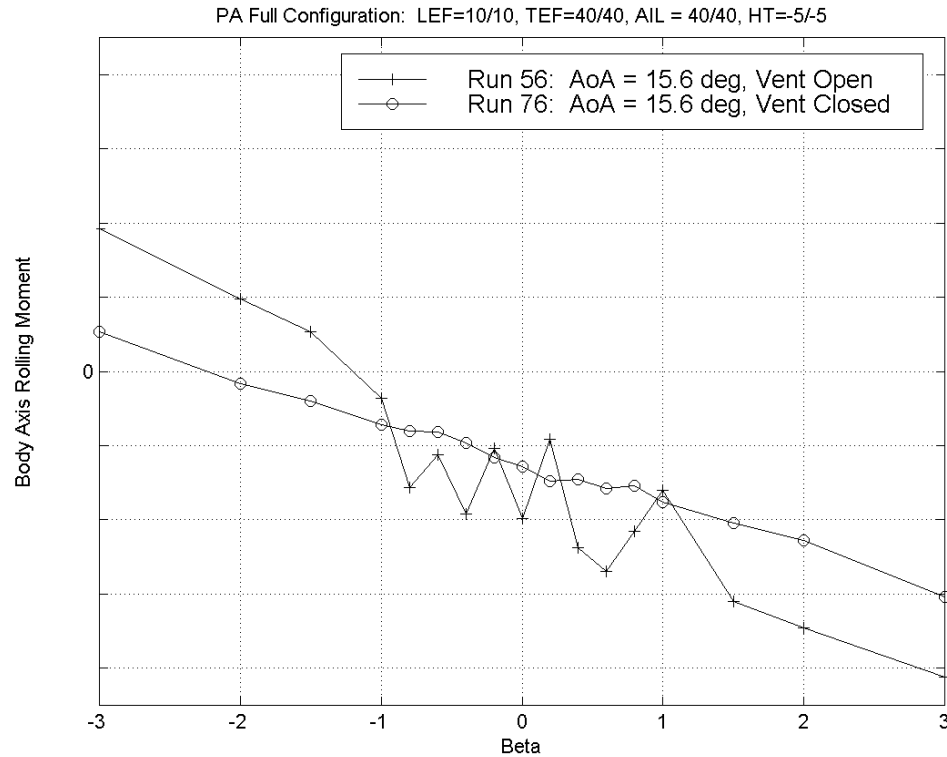


Figure 14 Wind tunnel β sweep of aircraft showing C_l' versus β .

data, but has the same slope. At large positive sideslips, the vent-open rolling moment again has the same slope, but now is more negative than the vent-closed data. This erratic behavior about zero indicates that the flow solution is very unstable and suggests a mechanism by which a symmetric model may exhibit asymmetric moments in a symmetric freestream flow.

Finally, the wind tunnel study was valuable in demonstrating the sensitivity of results upon leading edge flap (LEF) deflections. Figure 15 shows the relationship of this asymmetry with LEF deflection. Four different flap settings were tried in the wind tunnel, and in each case, the asymmetric rolling moment still occurred. However, when the angle of flap deflection increased, the asymmetry occurred at a higher angle-of-attack ranging from 14° with no flap deflection to 20° at 30° flap deflection. This figure also

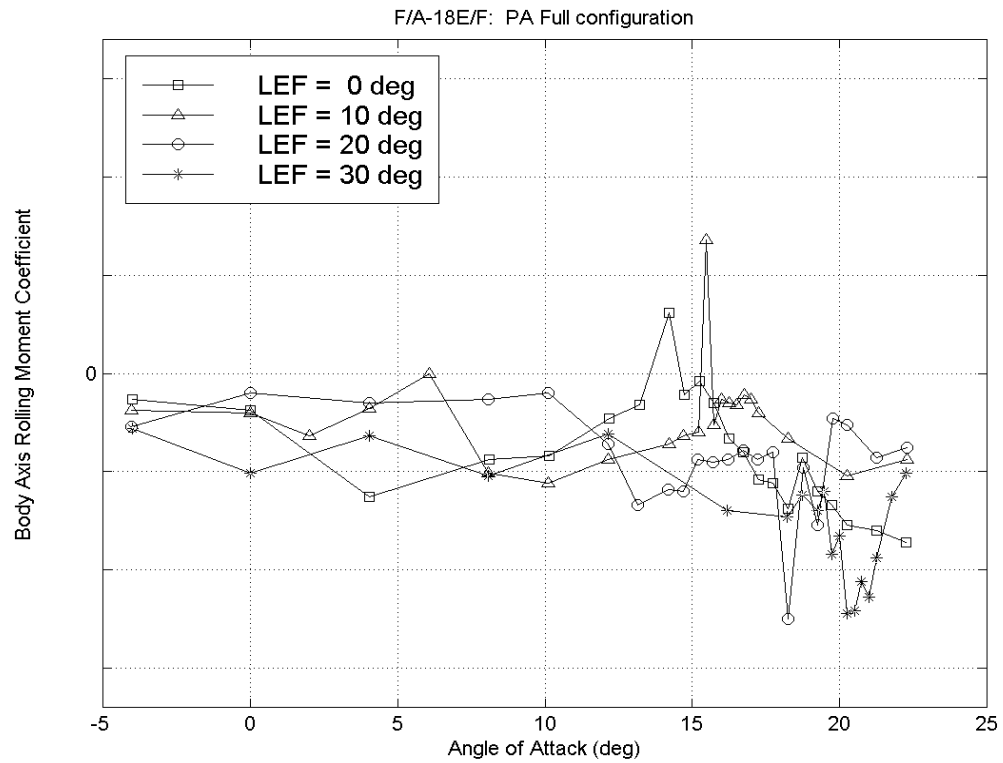


Figure 15 Wind tunnel data showing the effect of different LEF positions.

shows how the asymmetry can occur in either direction and is not specific to inducing a positive or negative rolling moment. Therefore the existence of the wing drop did not depend upon LEF deflection, and the effect was limited to influencing the angle-of-attack at which the drop might occur.

2. MODEL LIMITATIONS

The PA wing drop first occurred during early flight testing of the F/A-18E. As mentioned earlier, the exact cause of this phenomenon has not been understood. Thus, in order to find the most accurate solution using CFD, the computer model used should be as close to an exact geometrical representation of the actual aircraft as possible. However, some simplifications of the geometry were necessary to cut down the required computational time. Thus, there are many differences in geometry between the CFD model used and the actual aircraft used in flight testing. These differences are described below:

A. The aircraft used in flight test had slotted flaps with fairings, brackets, and a fully open cove. The computer model used a flap with no fairings, actuators, or brackets, and the cove was eliminated. The fairings and brackets added unnecessarily to the complexity of the geometry and the size of the grid. The flap slot likewise introduced tremendous grid size.

Wind tunnel testing validated the legitimacy of these simplifications. The wind tunnel model did not have any fairings or brackets connected to the flaps and ailerons. Furthermore, the model was tested both with the slot open and with the slot closed. The asymmetry still occurred in both cases, demonstrating that the wing could be legitimately modeled with a closed slot and no brackets or fairings.

B. The flight test where asymmetry was first discovered included the landing gear extended. Due to the complex geometry and the absence of a computer model of the landing gear, the landing gear was omitted from the computer model. Likewise, wind tunnel testing did not model the landing gear. Since the wing drop characteristics were still present in the wind tunnel data, the decision to omit the landing gear from the computational model was validated.

C. On the actual F/A-18E aircraft, the leading edge flaps (LEF) operate on a schedule based on the angle-of-attack on the aircraft. Accommodation of the LEF

schedule in the CFD study would have resulted in an enormous growth in the complexity of the study; a completely different grid would be required for each LEF position, and hence a different grid for each separate flight condition. Variations in the LEF schedule were among the first attempted fixes in flight test, and they showed that the wing drop occurred over a range of leading edge flap deflections between fifteen and thirty-one degrees. The LEF position affected only the angle-of-attack at which the wing drop occurred. The computer model obtained from Boeing had a fixed leading edge flap deflection of 20° , falling within the range in which the asymmetry is expected. Furthermore, wind tunnel testing was performed with a range of fixed LEF deflections, confirming that the deflection angle of the leading edge flap does not affect the presence of the rolling asymmetry. Likewise, the tunnel data revealed that the LEF deflection only changed the angle-of-attack at which the asymmetry first appeared.

Consequently, the only anticipated impact of the single LEF deflection on the CFD results is a variation in the angle-of-attack at which the wing drop is observed. The crucial information expected from the study is the variation in rolling moment with angle-of-attack. The significant gradients in the rolling moment with changes of angle-of-attack are behind the wing drop. Thus, only the presence of these gradients and their magnitudes are important, whereas the angle-of-attack at which they occur is not.

D. The CFD study used a half-model of the aircraft to halve the size of the grid and reduce the computational effort. The computer model assumes a symmetrical airflow over the aircraft with a reflection plane along the plane of aircraft symmetry. Since the wing drop is due to asymmetric rolling moment, it might appear that the half-plane model could not adequately model the flow.

The asymmetric rolling moment responsible for the wing drop is due to differences in the flow pattern between the two wings. Both flight test and wind tunnel data indicate that the flow does not vary smoothly with changes in angle-of-attack but abruptly jumps from one pattern to another. The wing drop was therefore attributed to

non-simultaneous jumps in the flow on the two wings, triggered by minute turbulence variations side-to-side, rather than cross-flow through the plane of symmetry.

Furthermore, the wing drop occurred both in flight and in the wind tunnel at a wide range of sideslip angles, with no correlation between the sideslip direction and the direction of wing drop. Thus, the half-model accurately represents the airplane for this project.

In one important sense, the half-model is analytically superior to a full model. This is due to the ability to isolate the variation in moment contributed by a single wing. The wind tunnel and flight test results only provide the net moment (i.e., sum of rolling moment contributions from each wing). Zero net rolling moment means only that the rolling moment contributions from each wing balance each other. This provides little information regarding the variation of the moment contribution from each wing. The half-plane model provides this information from a detailed analysis of the moment contribution from a single wing,

E. The configuration of the flight test aircraft and the wind tunnel model included a wing-tip launcher and AIM-9 Sidewinder missile. Due to the complexities that a full missile model would have on the CFD grid, the missile fins were left off from the computer model. The launcher and missile body were modeled because they significantly affect the flow field around the outer wing, and the aircraft never flies without at least a launcher. The missile fins themselves, however, were assumed to have insignificant effects and deleted for the sake of model complexity and node count. The validity of this assumption was affirmed by the wind tunnel results.

F. Owing to the problems which occurred in generating a viscous grid, the viscous grid was abandoned, and an inviscid grid was built. This makes some significant assumptions about the flow over the aircraft, especially over the trailing edge flap.

First, comparing the trends from the wind tunnel with the CFD will test the validity of this assumption. Both the C_L versus α trends and the qualitative character of the separated regions on the upper wing surface should be expected to agree for the

results to be accepted. These data will be presented in the next section.

Second, vortex lift research at the University of Maryland indicates that inviscid computational solutions compare favorably with viscous computations when used to model the effect of strong vortices off highly swept surfaces (such as the LEX).¹² This helps to further validate the inviscid assumption.

VI. RESULTS

1. NUMERICAL DATA

All data were obtained using inviscid Euler calculations. Solutions for flows at six different angles-of-attack ranging from 12° to 17° in one degree increments were obtained. Solutions were found for both the LEX vent-open configuration and the LEX vent-closed configuration, with the stabilator set to its neutral position. The characteristics of the final grids and the criteria for convergence of these solutions can be found in Appendix C. The flow solver determined the flow characteristics at each node in the entire grid. This data was then imported into VigPlot to allow for a visualization of the results.

Along with this flow data, USM3D integrated the forces and moments over the entire half-aircraft configuration and over a buildup of selected aircraft components. In order to understand the contribution of each component, this integration was performed on the inner wing panel, the outer wing panel, and the horizontal stabilator. The inner wing panel was that area defined from the junction of the LEX with the fuselage out to the leading edge snag, excluding the trailing edge flap. The outer wing panel was defined from the snag out to the wingtip, excluding the aileron. Coefficients of lift, pitch, and roll for each component were obtained from this integration. All the coefficients obtained from the integration can be found tabulated in Appendix D.

Figure 16 depicts a comparison of the lift curves of the vent-open configuration with the vent-closed configuration. The two lift curves are very similar until 14° angle-of-attack. For angles-of-attack 15° and 16° , the vent-open configuration lift curve departs from the traditional shaped lift curve and drops. A negative slope is evident for these

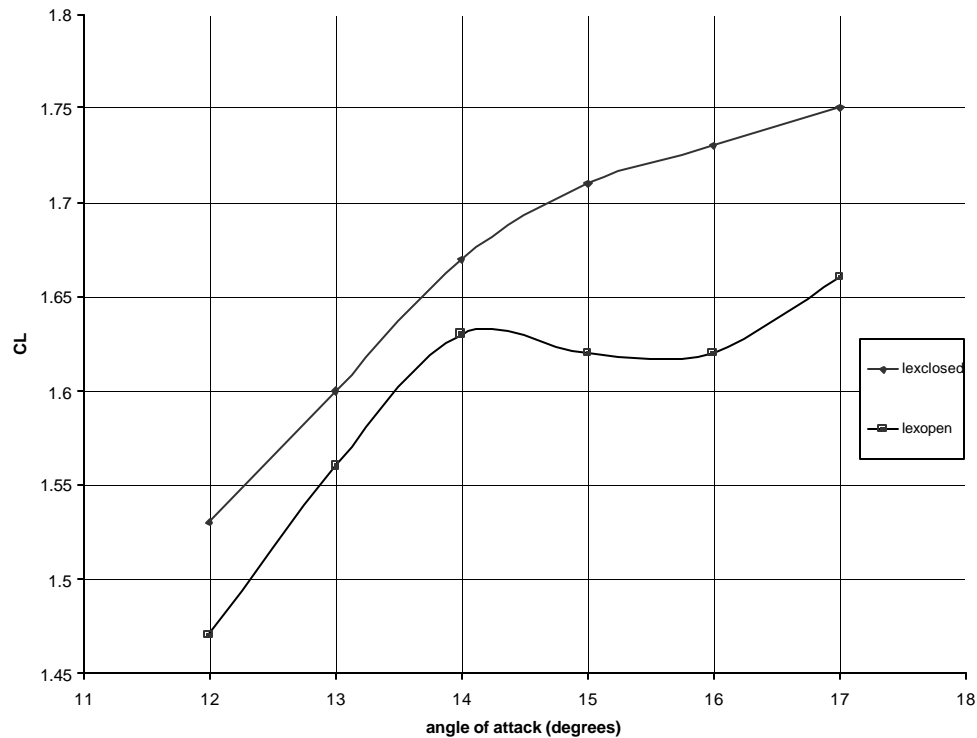


Figure 16 Lift curve of entire aircraft showing presence of wing drop.

angles-of-attack. At 17° angle-of-attack however, the lift curve reverses direction and begins to increase in value again, corresponding well with the wind tunnel data. Although the numerical magnitudes are different, both the computational data and the wind tunnel data exhibit the same drop in the lift curve for the vent-open configuration. Both lift curve slopes exhibit the same sign reversal and then continue to follow the original pattern.

Next, the lift coefficients of individual components were analyzed to see specifically which components were exhibiting signs of the lift loss. Figures 17 and 18 depict the lift curve for the inner wing and the outer wing. The outer wing lift contributes approximately the same lift for both the vent-open and vent-closed configurations. There

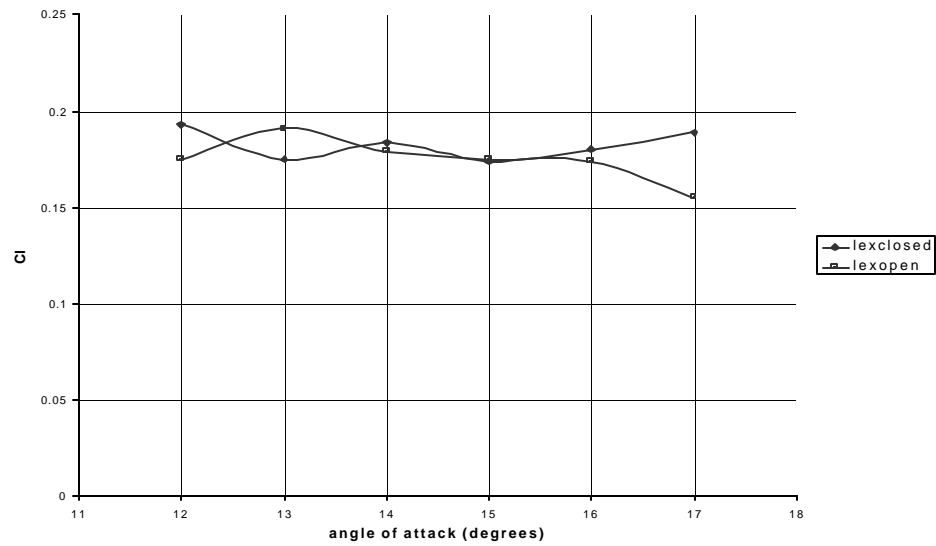


Figure 17 Lift curve of outer wing.

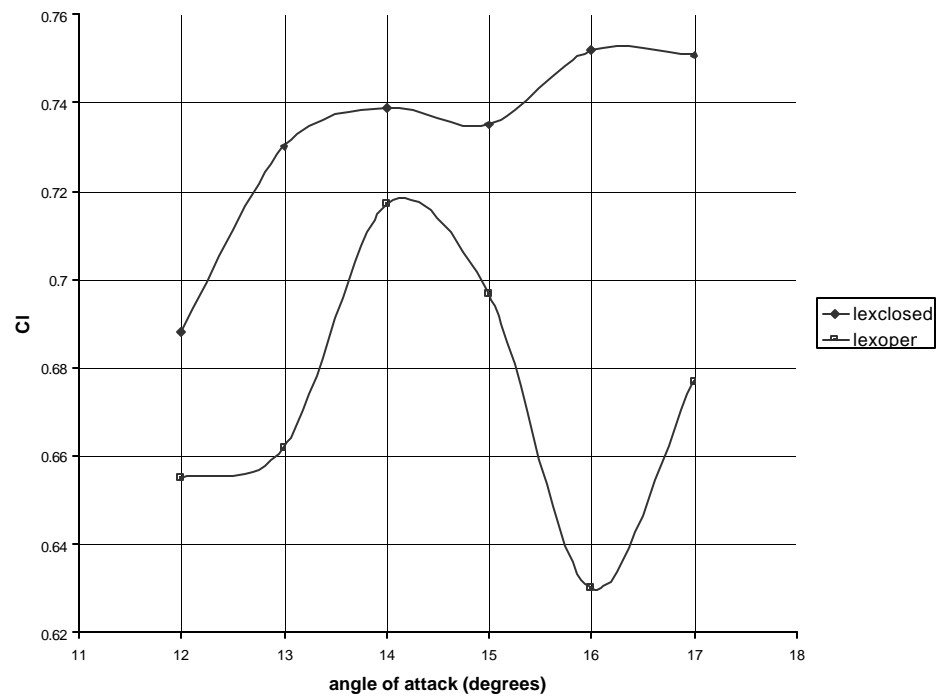


Figure 18 Lift curve of inner wing.

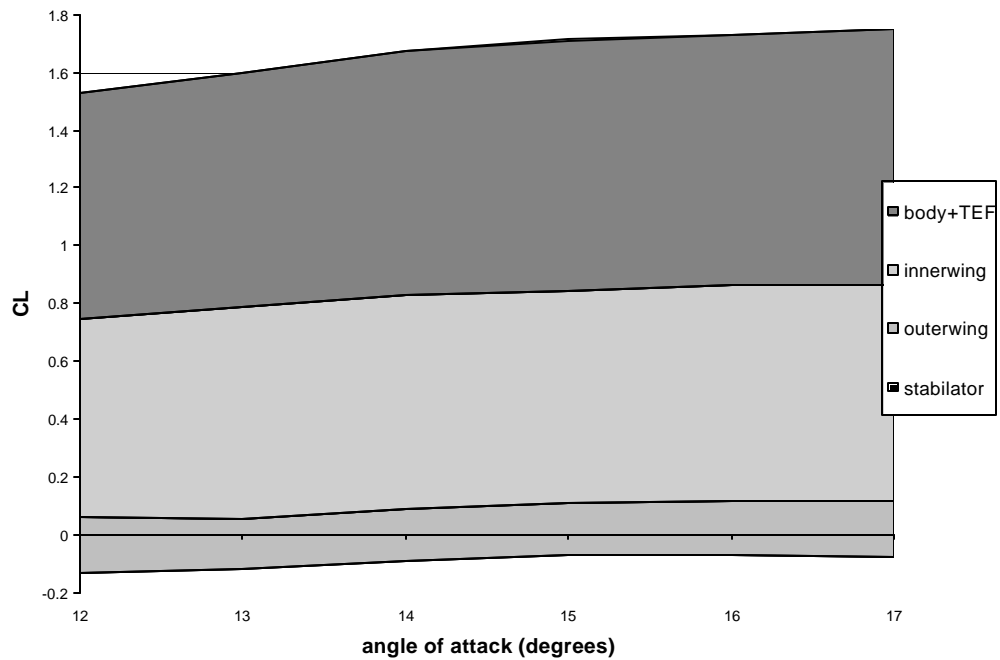


Figure 19 Component lift buildup for vent-closed configuration.

is no real variation in the lift coefficient values. The inner wing, however, shows a significant drop around 15° and 16° angle-of-attack. Before this point, the lift curves for the two configurations are similar. However, at 15° angle of attack, the two curves begin to diverge and the lift curve for the vent-open configuration drops suddenly, reaching its lowest value at 16° angle-of-attack, 12% below its peak contribution. Consequently, the major drop in lift occurs over the inner wing of the aircraft, but not the outer wing.

When a full lift buildup analysis is done on the aircraft, one observes that the inner wing produces almost half of the lift of the entire aircraft while the outer wing's contribution to the aircraft's lift is very small. Thus, the disturbance in the lift curve of the inner wing has a significant effect on the entire lift of the aircraft and is responsible for the drop in the lift curve. Figures 19 and 20 show the lift buildup for the entire

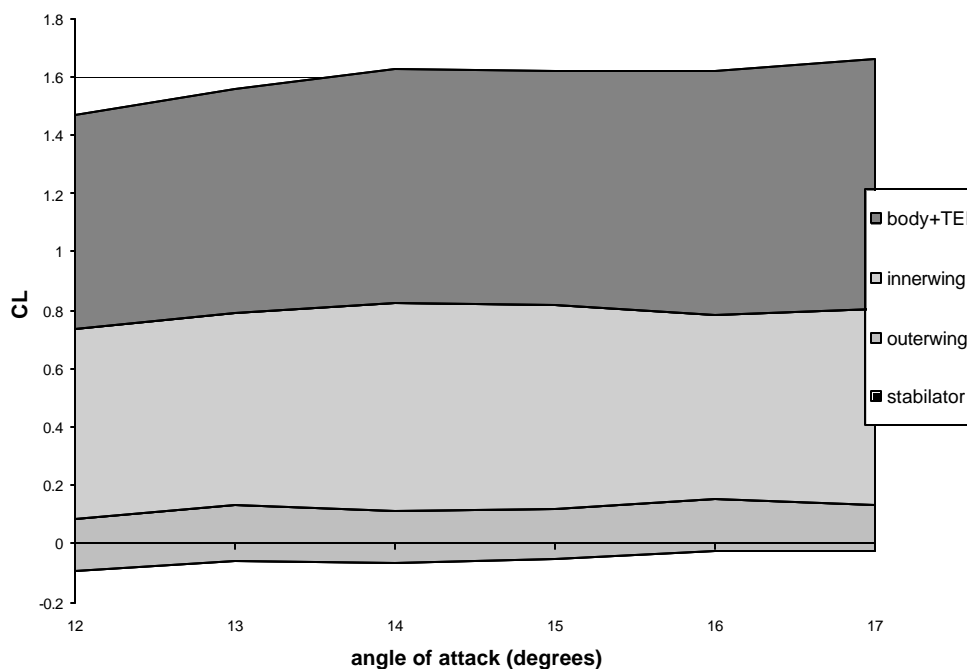


Figure 20 Component lift buildup for vent-open configuration.

aircraft. The bottom line is negative since the stabilator's lift contribution is negative due to the downwash on the tail. The other components then add to that original negative base.

From these figures, it is evident that the inner wing is responsible for over three times the lift of the outer wing. The vent-closed configuration shows a smooth increase in the lift of all the major components. The vent-open configuration, however, shows a significant drop in the amount of lift the inner wing is producing at 16° angle-of-attack.

The stability-axis rolling moment also shows the presence of the wing drop. Figure 21 depicts the rolling moment, C_l' versus α , for the half-plane model. Because this is a half-model, the rolling moment increases as the lift on the aircraft increases. However, between 14° and 16° angle of attack, the rolling moment on the vent-open

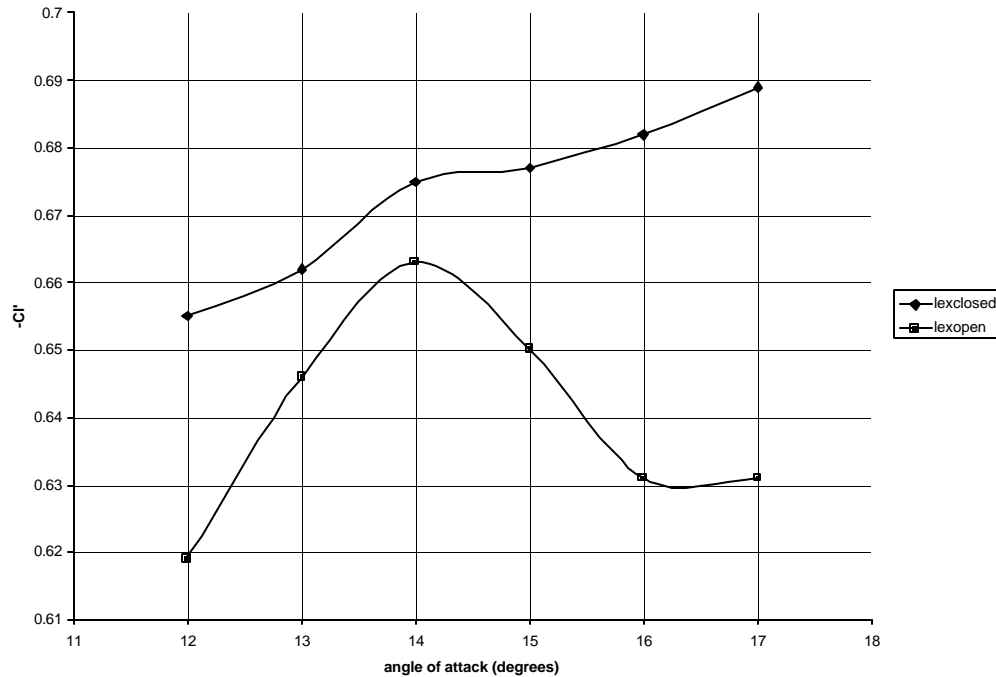


Figure 21 Difference in aircraft rolling moment between the two configurations.

configuration reverses, decreasing sharply. The magnitude of this disparity is also important. Even though the total aircraft lift only dropped by 1%, the half-plane rolling moment dropped by 5%! This shows how the effects of a slight change in lift can be amplified to affect the aircraft rolling moment significantly.

The above result explains how a very small loss of lift on one wing is capable of producing a significant unbalanced moment if the drop on the two wings does not occur simultaneously. Follow-on research needs to be performed to ensure that the computed magnitudes of both the lift and moment are consistent with wind tunnel and flight test.

Beyond the above qualitative results, the question still remains, “What feature of the flow is responsible for such drastic differences between the two configurations?” The next section will attempt to address this using flow visualization.

2. FLOW VISUALIZATIONS

All the data presented up to this point have been quantitative. These data matched the wind tunnel data closely. They also confirmed the presence of the wing drop and established that the asymmetry occurred over the inner wing. Along with the numerical data obtained from the flow solver, many flow visualizations were obtained from the computer program VigPlot. These visualizations help to show in a qualitative manner the cause of the lift loss over the inner wing. Since all of the visualizations are animation sequences, they can best be viewed electronically. For the purpose of this report, however, samples of these animations can be found in the text, with the entire sequences located in the Appendices. Each of these visualizations represents both vent-open and vent-closed configurations. Since both configurations were a right-wing configuration, the solution for the vent-open case was mirrored to produce a left-wing result. This was combined with the right-wing solution for the vent-closed configuration to produce a whole aircraft with one wing in each configuration for easy analysis. All of the visualizations are broken down into two categories: On-body and off-body flow representations.

A. On-Body Flow Analysis

When looking at the pressure distribution on the surface of the aircraft, a difference in the flow patterns over the wing can be found between the vent-open and vent-closed configuration. Figure 22 shows a top-down view of the aircraft surface pressure distribution at 12° angle-of-attack. The vent-open configuration is the left wing and the vent-closed configuration is the right wing of the aircraft. The colors are based on pressure values with reds and oranges being areas of high pressure and blues and greens

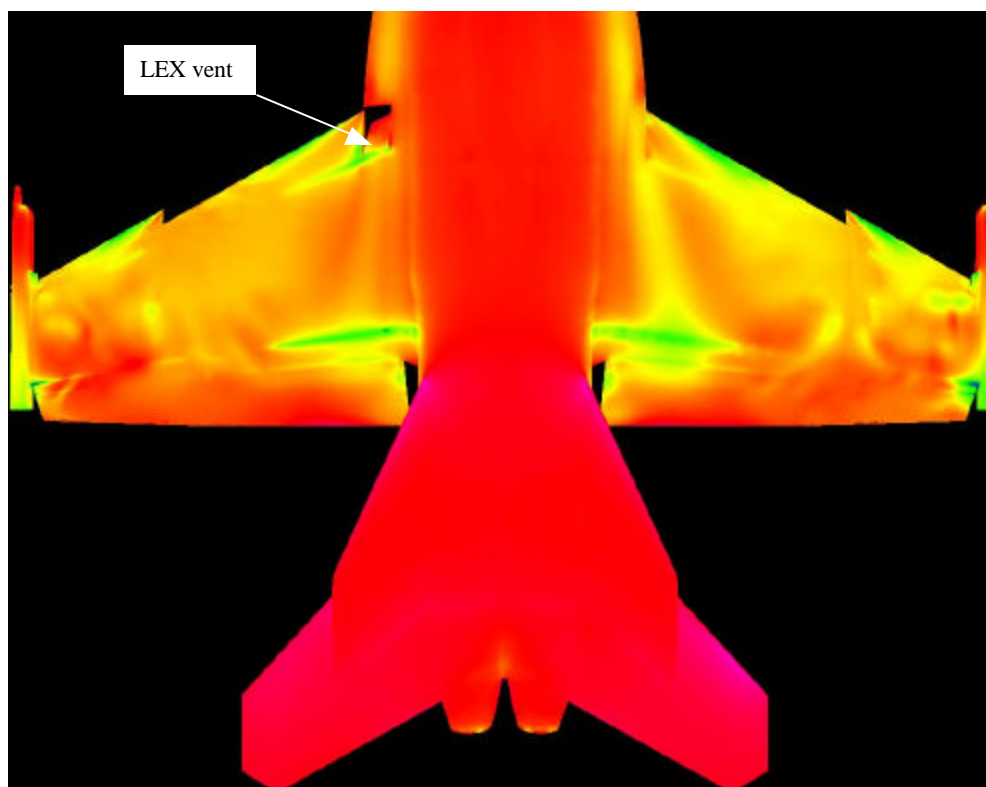


Figure 22 Surface pressure distribution on aircraft at 12° angle-of-attack.

being areas of lower pressure. Since a pressure difference between the upper surface of the wing and the lower surface of the wing is what creates lift for an aircraft, the areas of lower pressure (blue) on the top surface provide more lift than those areas of higher pressure (red).

The outer wings appear to be very similar in terms of the pressure distributions. The inner wings of the two configurations are similar but do reflect a distinct difference close to the fuselage, directly aft of the LEX. A strong region of low pressure runs chordwise aft of the LEX in the vent-closed configuration. However, in the vent-open configuration, that chordwise stream of low pressure does not exist. Conversely, a stream of pressure higher than the surrounding area exists in its place.

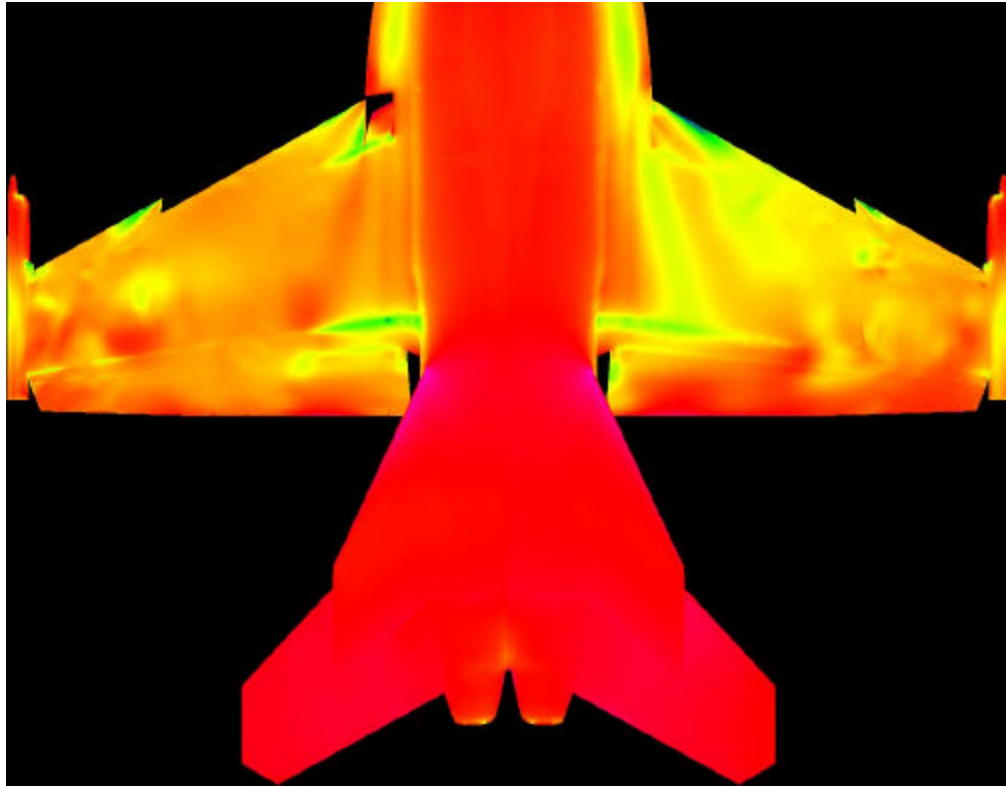


Figure 23 Surface pressure distribution on aircraft at 16° angle-of-attack.

This phenomenon becomes more pronounced at a higher angle-of-attack. Figure 23 shows the pressure distributions for the two configurations at 16° (the angle-of-attack at which the quantitative data indicated a lift loss). Again, the outer wings of both configurations are very similar. However, a large disparity now exists between the two inner wing panels. The low-pressure stream running aft of the LEX on the vent-closed configuration is much larger and much more prominent. It appears to be very influential on the rest of the inner wing. The vent-open configuration still does not have this pronounced low-pressure stream, with most of the wing at a comparatively high pressure.

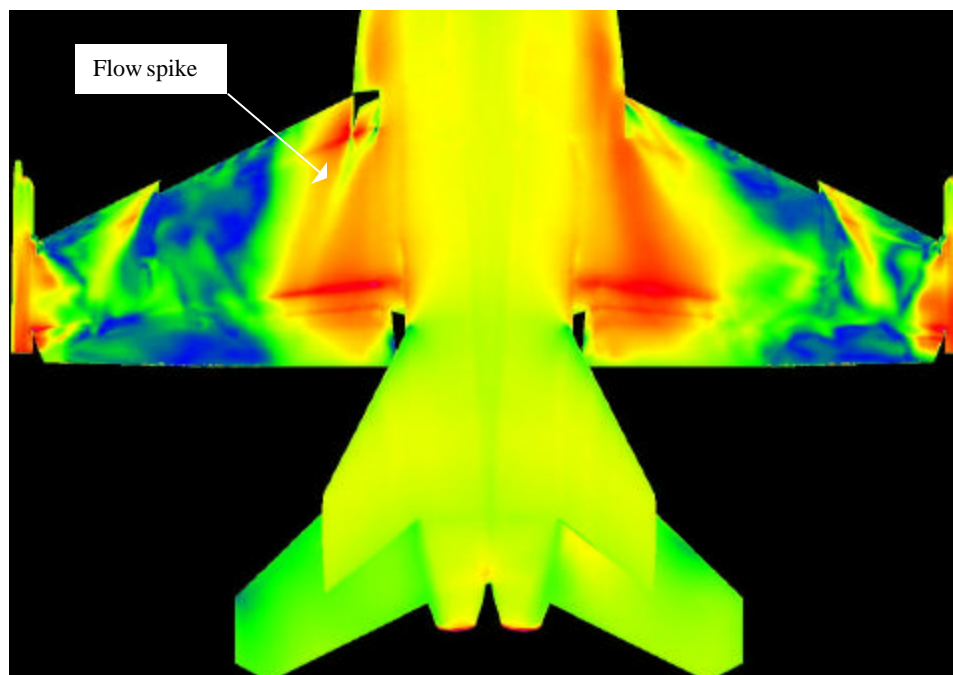


Figure 24 Surface Mach number distribution at 12° angle-of-attack.

This phenomenon can also be seen in the Mach number distributions over the surface of the aircraft. Figure 24 depicts the surface Mach number distribution at 12° angle-of-attack. The blue color represents a Mach number of almost zero, while the reds and oranges represent higher Mach numbers. The velocities are taken in the u , or flow direction. Faster flows over the upper surface of the wing create lower pressures and thus more lift. Regions of slower flow indicate higher pressure regions, and thus less lift. The areas where the velocity is zero indicate reverse flow areas where no lift is being produced. Again, the outer wings have similar flow patterns, however the inner wings are vastly different. Besides the fact that there is a larger reverse flow region on the vent-open configuration, there is a spike of lower Mach number originating from the LEX vent and traveling chordwise aft. On the vent-closed configuration, there is a large high Mach

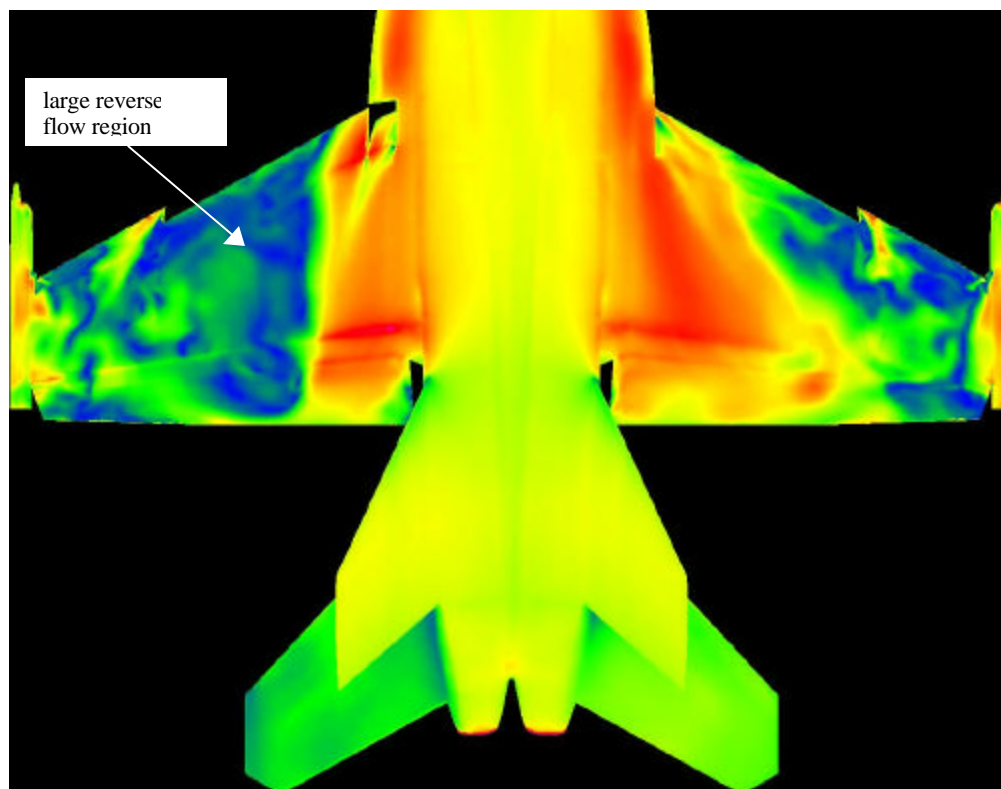


Figure 25 Surface Mach number distribution on aircraft at 16° angle-of-attack.

number region in place of the spike of the vent-open configuration.

Figure 25 depicts the Mach number distribution at 16° angle-of-attack. On the vent-closed configuration, the region of high Mach number has enlarged and become stronger, correlating with the increased quantitative lift distribution from this wing panel. This region has a large effect on the entire inner wing and helps to keep the flow attached. Because of the existence of the spike in the vent-open configuration, this area of high Mach number does not exist and thus does not have a very strong influence over the rest of the inner wing. Therefore, most of the inner wing is in reverse flow. The outer wings once again are alike in both configurations.

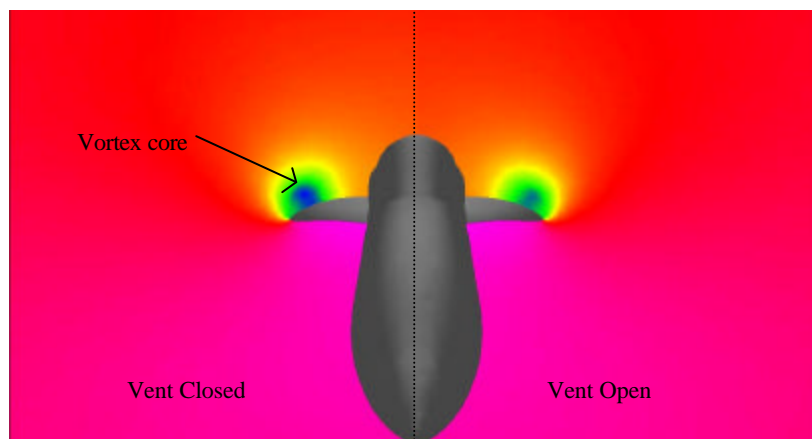


Figure 26 Off-body pressure distribution at 12° angle-of-attack.

2. Off-Body Flow Analysis

The previous visualizations help to describe the flow over the aircraft's surface. However, in order to fully understand what is happening with the airflow, the airflow properties off-body must be analyzed as well. This is where the limitations in wind tunnel research become evident, where off-body airflow properties are difficult and expensive to obtain. CFD, however, allows for a detailed analysis of the flow surrounding the aircraft, not just on the aircraft's surface.

Pressure is an interesting off-body flow property to analyze, especially the pressure variance in the yz plane (the plane perpendicular to the longitudinal axis). The program VigPlot created an animation showing the pressure distribution in the yz plane starting forward of the wing, and stepping aft in 10 inch intervals, finishing just aft of the trailing edge flap. This entire animation sequence can be viewed in Appendix D.

Figure 26 shows the first slide of this animation. This is a head-on view of the aircraft at 12° angle-of-attack. The right side of the figure (aircraft's left wing) depicts the vent-open configuration, while the left side of the figure (aircraft's right wing) depicts the vent-closed configuration. Once again, the blues and greens represent areas of low

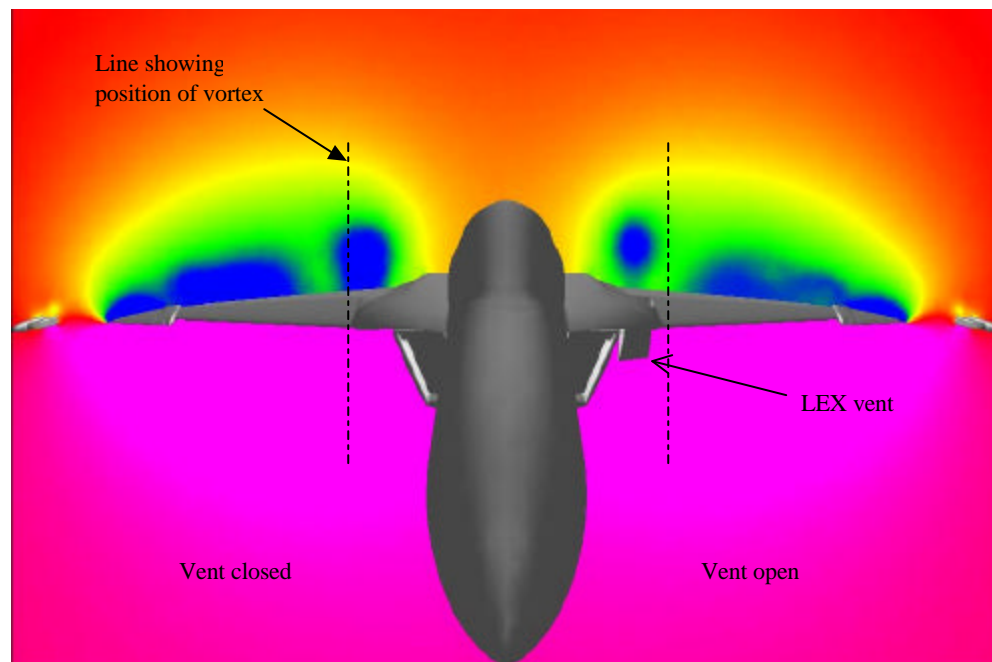


Figure 27 Off body pressure distribution showing differences in vortex characteristics.

pressure, while the reds and oranges represent areas of higher pressure. The yz plane sampled is at a location just before the leading edge flap and LEX vent. The circular areas of low pressure off-body represent vortex cores in the airflow. From this figure, one can not see much difference between the two configurations. Both vortices are located in approximately the same location over the leading edge extension. The vortex for the vent-open configuration appears to be slightly smaller (and thus weaker) than the vent-closed vortex.

This slight difference in the vortices becomes more distinct further aft. Figure 27 depicts the pressure distribution at a location close to the mean aerodynamic chord of the wing root, just aft of the wing snag. The vertical dashed lines provide a reference mark at a fixed spanwise location for comparison purposes. This figure illustrates many differences between the vent-open and vent-closed configuration. First, the vortex core is

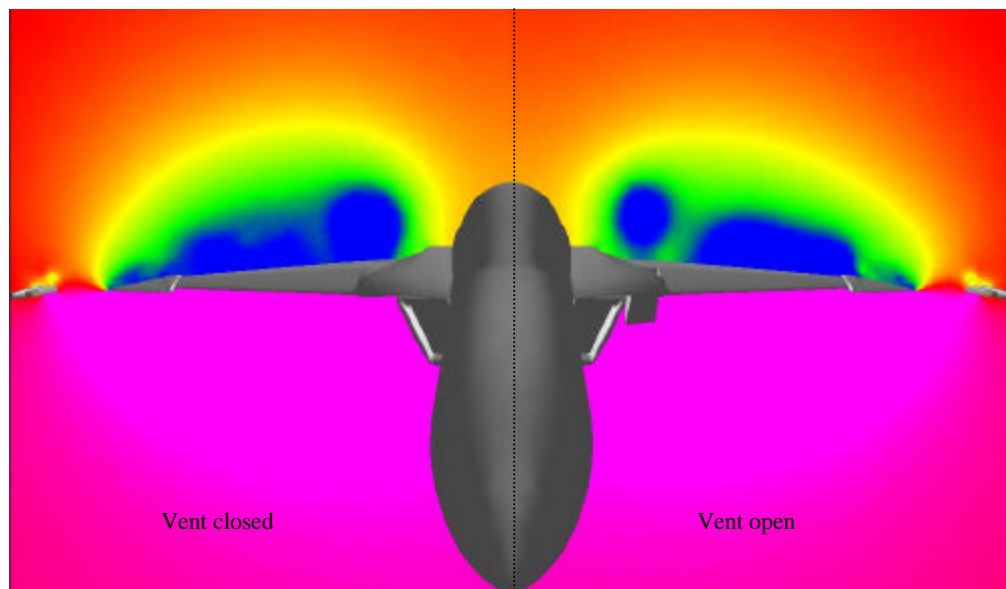


Figure 28 Off body pressure distribution at 15° angle-of-attack.

smaller and weaker on the vent-open configuration. It is also detached from the upper wing surface. This makes sense because the flow comes through the vent and blows the vortex up off from the body.

Furthermore, it also becomes evident that the vent-open vortex is located closer to the centerline of the fuselage. The vent-closed vortex appears centered over the LEX/leading edge flap junction, while the vent-open vortex appears centered further inboard. It can also be seen from the entire animation sequence that aft of the trailing edge flap, the vent-closed vortex is still present, however, the vent-open vortex has dissipated.

A second animation sequence depicts the variation of these pressure distributions with angle-of-attack, by fixing the chordwise location of the yz plane and varying the angle-of-attack. The full animation sequence can be found in Appendix E. Figure 28 represents the pressure distribution at 15° angle-of-attack.

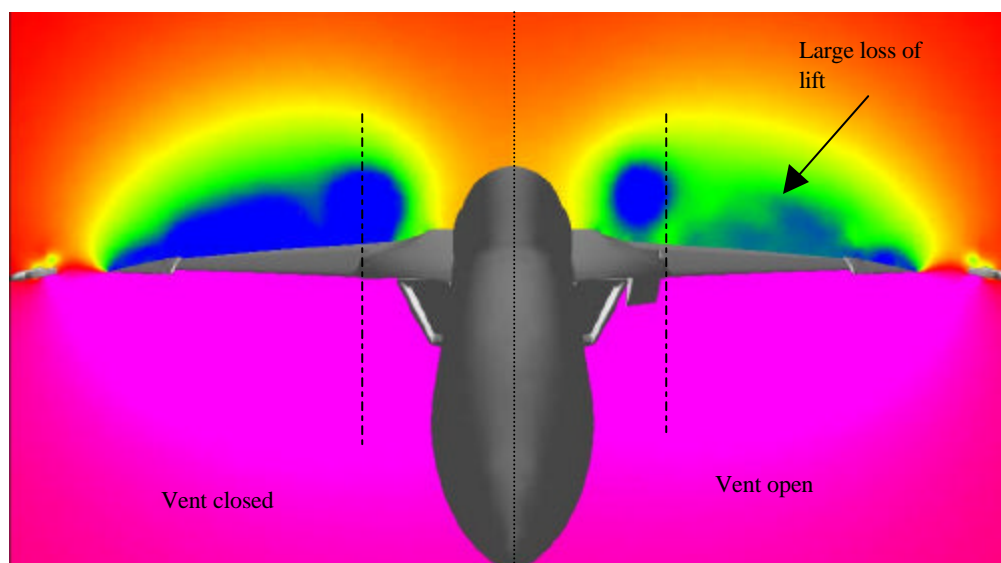


Figure 29 Off-body pressure distribution at 16° angle-of-attack.

Many interesting features deserve note. First, both of the vortices are much larger than at 12° (Figure 27). The area of low pressure over the wing is much larger. This makes sense, given the increased lift at this angle-of-attack. Once again, the vent-open vortex is closer to the fuselage centerline and is separated vertically from the upper wing surface. It is also distinctly removed from the inner wing's low-pressure bubble, where it has no influence over the inner wing lift. In contrast, the inner wing bubble the on vent-closed configuration is connected with the vortex. Thus, the vortex has a strong influence over the inner wing's lift.

Figure 29 shows the pressure distribution at 16° angle-of-attack, the angle of attack at which the drop in the lift curve was most severe. This figure explains this lift loss. Vent-open, the low-pressure bubble over the inner wing has vanished, attributable for the drop in the lift curve. A large, powerful vortex remains, but is vertically displaced from the surface and horizontally isolated from the lift bubble on the inner wing panel. In

contrast, vent-closed displays a dramatically different character. The vortex has swollen further and is now both directly providing lift on the inner wing panel and communicating with the remainder of the lift bubble.

3. SUMMARY OF RESULTS

Matching the wind tunnel results, the lift curve of the vent-open configuration exhibits a characteristic drop between 15° and 16° angle-of-attack. This lift loss comes primarily from the inner wing, and the lift of the inner wing composes almost 50% of the entire lift of the aircraft. The vortex of the vent-open configuration is smaller, weaker, and is closer to the fuselage centerline having a very small influence over the lift on the rest of the wing. The vortex is also driven up off from the wing surface causing the spike in the surface Mach number and the higher pressure in the surface pressure distribution. When the angle of attack of the aircraft is varied, the vortex cores grow, as well as the areas of lift over the wing. However, the vent-open lift grows independently of the vortex while the vent-closed lift grows with the vortex. At 16° angle-of-attack, a sudden loss in lift occurs over the inner wing in the vent-open configuration, showing the characteristics of the wing drop phenomenon. Since the F/A-18 Hornet relies heavily on these vortices to provide the majority of its lift, the vortex disturbances discussed above can have a significant effect on the controllability of the aircraft.

VII. FUTURE RESEARCH

Many simplifications were made in modeling the aircraft in order to complete the current research, leaving many avenues open that will help to provide an even better understanding of this wing drop phenomenon.

The first thing that should be done is a β -sweep using the current configuration. Wind tunnel testing demonstrated that a β -sweep done on the vent-open model showed interesting fluctuations in the aircraft rolling moment not present on the vent-closed model. This would involve modeling the entire aircraft, thus doubling the size of the grid and raising the computational time needed to achieve a solution by a factor of four to eight. This analysis would have to remain inviscid, as making the half plane model viscous enlarges the grid by another factor of two to three.

Second, another project would be to open the slot in the trailing edge flap. This is needed for two main reasons. (1) A slot-open model is a prerequisite to a viscous solution. The flow would not make sense if a viscous solution were attempted without the slot open. (2) The slot is also a prerequisite to a stabilator sensitivity analysis. The flow through the slotted flap helps to define the downwash on the stabilator, thus directly affecting the stabilator's sensitivity.

Once the slot is opened, then a full viscous Navier-Stokes analysis should be done. This will provide the most accurate flow representation for the aircraft. However, the grid size from this model will be on the order of 4–5 million cells and take a much longer time to generate a solution. In order to do this, a new grid generator may have to be used, as the one currently being used may not be able to model this complex geometry fully in a viscous grid.

For each of these projects, more angles-of-attack should be run as well. Only solutions for 6 different angles-of-attack were found for this research due to time constraints. However, it would be beneficial to broaden the range of angles of attack and decrease the increments as well, providing a more sensitive analysis of the wing drop phenomenon.

VIII. REFERENCES

1. Heller, Michael J. and Hoy, Stephen E. "F/A-18E/F Flying Qualities Report Volume II: High Angle of Attack Flying Qualities - Flight Test Basis." 4 Oct 99. The Boeing Company, St. Louis, MO.
2. Bose, T.K. Computational Fluid Dynamics, John Wiley and Sons: New York, 1988. pp 1-5.
3. Anderson, John D., Jr. Modern Compressible Flow, McGraw Hill: Boston, 1990. pp 307-311.
4. Anderson, John D., Jr. Fundamentals of Aerodynamics, McGraw Hill: New York, 1991. p34.
5. <http://ad-www.larc.nasa.gov/tsab/tetruss/pubs.html>
6. Pope, Stuart and Viken, Sally. "Introduction to GridTool: An Interactive program for grid/geometry applications." June 1999.
7. <http://ad-www.larc.nasa.gov/tsab/tetruss>
8. Pope, Stuart and Viken, Sally. "VGRID Version 3.2 User Guide." June 1999.
9. Frink, Neal and Parikh, Paresh. "USM3d and VigPlot Training Material." June 1999.
10. Dodbele, S.S., Hobbs, C.R., Kern, S.B., Ghee, T.A., Hall, D.R., and Ely, W.L., "Wind Tunnel Experiments and Navier-Stokes Computations of a High-Lift Military Airfoil," AIAA 99-0540, January 1999.
11. Cook, Steve. Personal Interview. 23 September 1999.
12. Willams, Reginald Guy, Ph.D. "The Computational Investigation of Leading Edge Vortex Breakdown Over a Double Delta Wing Configuration," dissertation, University of Maryland, 1999.

IX. APPENDICES

APPENDIX A

SUMMER INTERNSHIP

The summer internship at Patuxent River NAS, and at NASA Langley Research Center was indispensable to this project. While at NASA Langley, I took a class on how to use the grid generation software. The entire process was explained in detail, and hands on instruction was done for each part. Once I returned to Patuxent River, I was able to apply what I learned on some sample geometries to become proficient and comfortable with using the software. The majority of the time spent at Patuxent River was in finding and assembling a workable, accurate, high-definition geometry of the F/A-18E. Without this time at Patuxent River during the summer, much time would have been lost at the beginning of the last semester trying to assemble an accurate geometry and in learning how to operate the grid generation software.

APPENDIX B

List of USM3D input file requirements

General Flow Characteristics:

Freestream Mach number (Mach)
Angle of attack (alpha)
Angle of side slip (beta)
Freestream Reynolds number (ReUe,mil)
Freestream static temperature (Tinf,dR)
Wall temperature (Tw/Tinf)
Reference area (sref)
Reference length (cref)
Reference span (bref)
X,Y,Z Coordinates of moment center (xmc,ymc,zmc)

Engine Specific Characteristics:

Number of jet engines (nengines)
Fuel fraction (fuel)
Ratio of specific heats (gamma_j)
Static nozzle pressure (p_{jet})
Stagnation pressure of jet (P_{0jet})
Specific gas constant ratio (R_{ratio})
Stagnation temperature of jet (T_{0jet})
Directional cosines of jet exhaust plane (vec(1), vec(2), vec(3))

Other Flow Solver Flags:

Flags that activate and regulate solver functions and processes

APPENDIX B

Sample USM3D Input File

```

USM51 - Lexopen Configuration - viscous Grid
Mach      alpha      beta      Re/inch      Tinf,dR      itwall      Tw/Tinf
0.17000    12.0000      0.00      0.1188      460.0        0           -1.0
sref      cref      bref      xmc      ymc      zmc
36000      157.2      250.98    476.800    0.00000      92.7950
impl      dt/cfl1      iramp      cfl2      cflmin      nstage      autocfl
1          -10.0        50         50.00      2.0         10          0
irest      mstage      iresmth      dqmax      ptol      frac_hit      limiter
1          3           1          0.25      0.001      0.001      1.
nupdate    nwrest      ipltqn      ifast      idiagnos      nodeypl
50         50         2          0         0         0
iorder     lapl-avg    high-bc      ifds      ivisc      ckv
0          2          1          1         0         0.25
ncyc       nengines    bcfile      compF&M      cldes
1          1          1          1         0.
jet1/core  fuel        gammaj      pjet      P0jet      Rratio      T0jet
102        .012        1.37       0.7143    2.0539     1.022      1.3223
jet1/core  vec(1)      vec(2)      vec(3)
102        1.0        0.0        0.0

```


APPENDIX C

Solution Convergence

The finished vent-open grid was composed of approximately 1.3 million tetrahedra, whereas the vent-closed grid was composed of 1.2 million tetrahedra. Running on an ORIGIN 2000 multi-processor, the jobs took nearly 20 hours to complete with 6-8 processors running in parallel. Each angle-of-attack was run for 1000 iterations before convergence was obtained. The criteria for convergence were based on the analysis of the value of the residual and the lift coefficient. After each iteration, USM3D tabulated the iteration number, the log of residuals, and the coefficients of lift and moment. The log of the residuals was the log of the ratio between the current residual and the initial residual. A continual drop in the log of the residuals characterized a converging solution. This was seen in a graph of the residuals over time. The lift and moment coefficients were also analyzed for convergence. A graph of these coefficients over time takes on the form of damped oscillations. When the amplitude of these oscillations is less than 0.5%, the numbers are considered to be nearing convergence. Figures C1, C2, and C3 depict the values of the log of the residual, the lift coefficient, and the moment coefficient over time for the vent-open 12° case. These graphs are representative of all of the solutions.

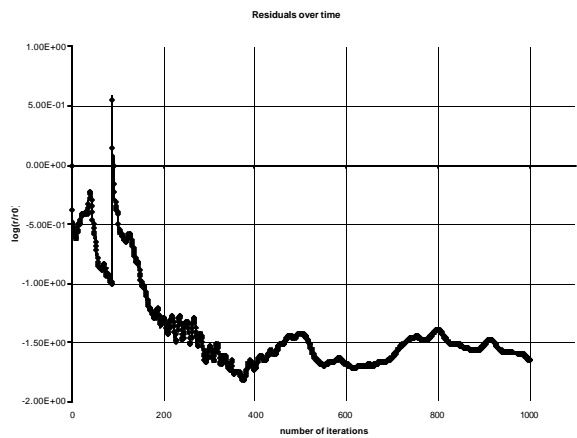


Figure C1. Residual plot over time.

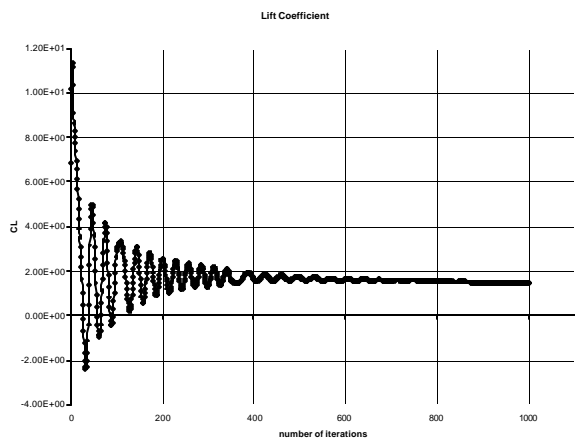


Figure C2. C_L variance over time.

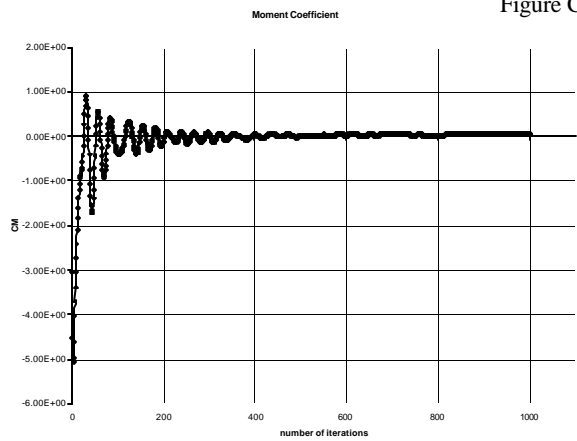


Figure C3. C_M variance over time.

APPENDIX D

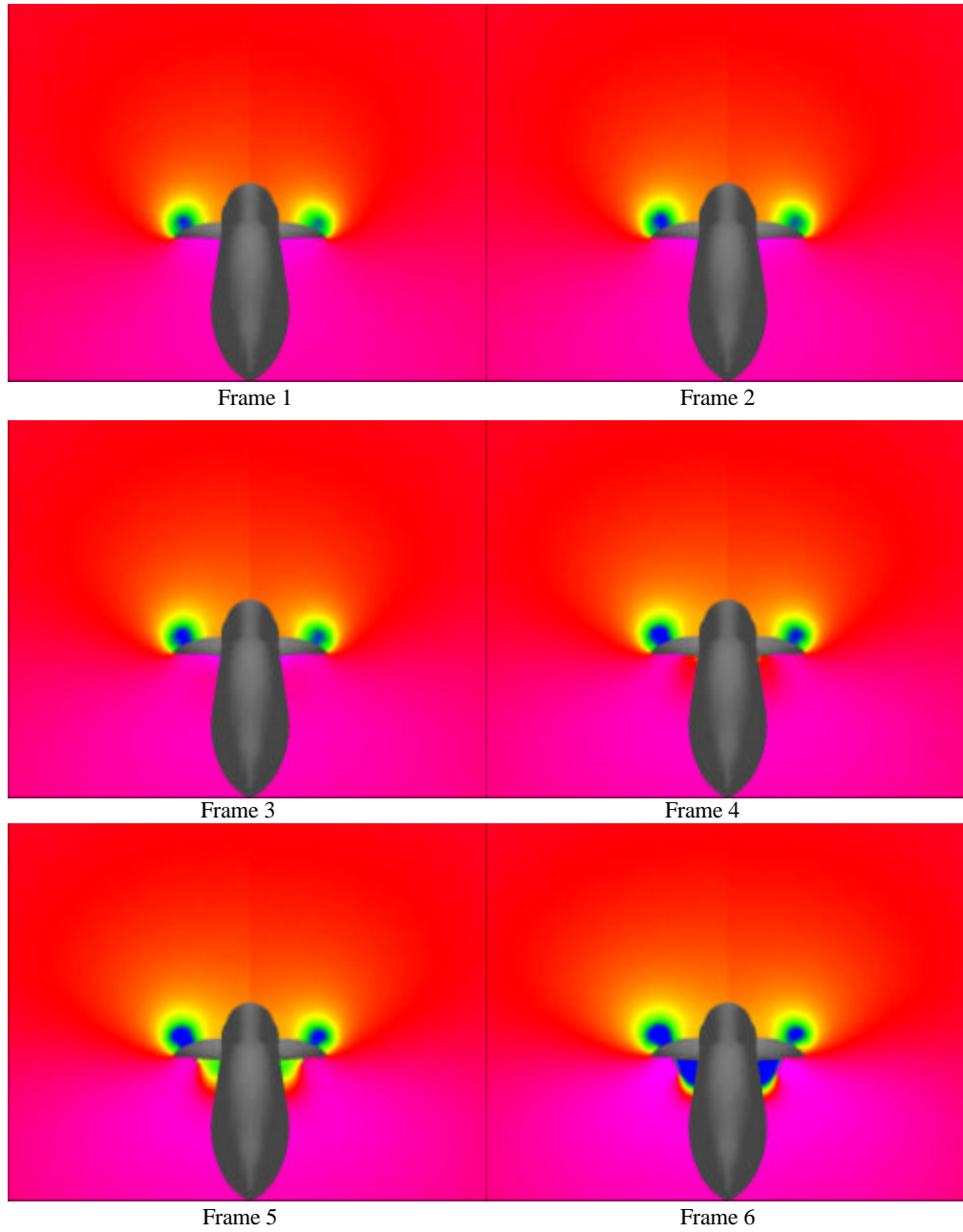
Coefficients Obtained From USM3D Flow Solver

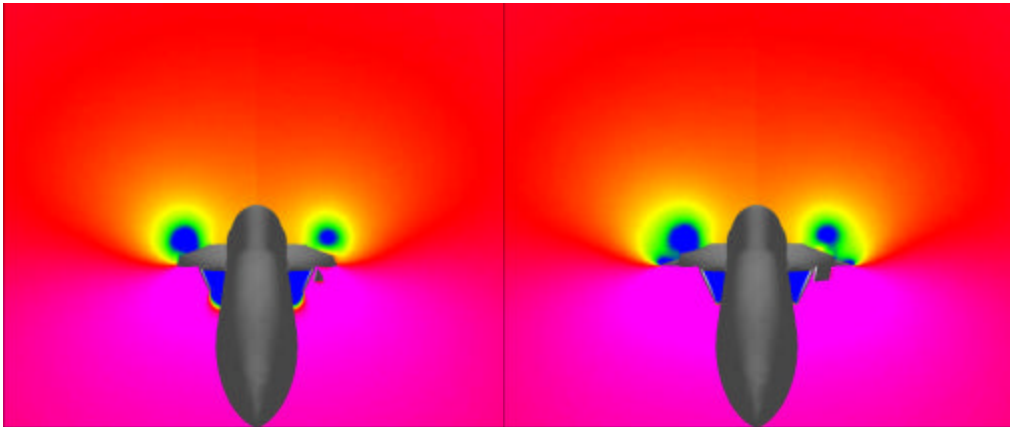
LEXCLOSED								
alpha	TOTAL AIRCRAFT				STABILATOR			
	Cl	Cd	Cpitch	Croll	Cl	Cd	Cpitch	Croll
12	1.53	0.464	0.0924	-0.655	-0.132	-0.029	0.197	0.0497
13	1.6	0.51	0.0935	-0.662	-0.119	-0.0276	0.1743	0.0418
14	1.67	0.547	0.0728	-0.675	-0.0938	-0.0249	0.1384	0.0331
15	1.71	0.606	0.0427	-0.677	-0.0691	-0.0204	0.0954	0.0213
16	1.73	0.613	0.0825	-0.682	-0.0667	-0.0209	0.0959	0.0215
17	1.75	0.656	0.12	-0.689	-0.0768	-0.0254	0.11	0.0229
alpha	OUTER WING				INNER WING			
	Cl	Cd	Cpitch	Croll	Cl	Cd	Cpitch	Croll
12	0.193	0.023	-0.0591	-0.167	0.688	0.0935	-0.0972	-0.31
13	0.175	0.0245	-0.054	-0.1508	0.73	0.113	-0.105	-0.329
14	0.184	0.0305	-0.0585	-0.159	0.739	0.132	-0.108	-0.332
15	0.174	0.0332	-0.05664	-0.1498	0.735	0.146	-0.108	-0.328
16	0.18	0.0379	-0.0587	-0.155	0.752	0.161	-0.107	-0.337
17	0.189	0.0449	-0.0639	-0.165	0.751	0.174	-0.106	-0.335

LEXOPEN								
alpha	TOTAL AIRCRAFT				STABILATOR			
	Cl	Cd	Cpitch	Croll	Cl	Cd	Cpitch	Croll
12	1.47	0.438	0.0355	-0.619	-0.0907	-0.0191	0.1354	0.033
13	1.56	0.482	-0.00262	-0.646	-0.0595	-0.0135	0.0914	0.02276
14	1.63	0.531	0.0281	-0.663	-0.067	-0.0159	0.1017	0.0251
15	1.62	0.561	0.045	-0.65	-0.0534	-0.0154	0.0858	0.0195
16	1.62	0.62	-0.0017	-0.631	-0.0216	-0.00759	0.0394	0.00949
17	1.66	0.656	0.0296	-0.631	-0.0245	-0.00932	0.0385	0.00842
alpha	OUTER WING				INNER WING			
	Cl	Cd	Cpitch	Croll	Cl	Cd	Cpitch	Croll
12	0.175	0.0198	-0.0528	-0.1511	0.655	0.0937	-0.0956	-0.294
13	0.191	0.0272	-0.0601	-0.164	0.662	0.1063	-0.0956	-0.298
14	0.179	0.0311	-0.0578	-0.1549	0.717	0.126	-0.102	-0.322
15	0.175	0.0343	-0.0579	-0.152	0.697	0.136	-0.0981	-0.312
16	0.174	0.0347	-0.055	-0.151	0.63	0.139	-0.0913	-0.28
17	0.155	0.0379	-0.0528	-0.1348	0.677	0.161	-0.0997	-0.302

APPENDIX E

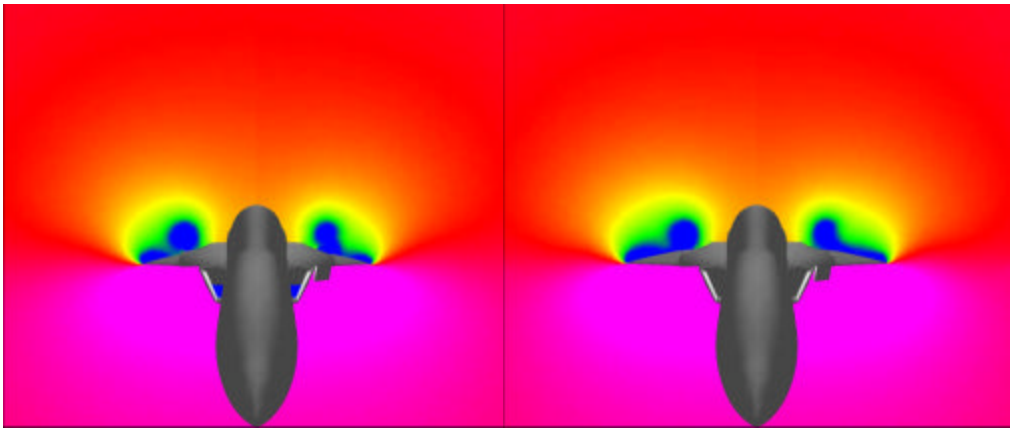
Animation Sequence Showing Stream-wise Progression of Vortices





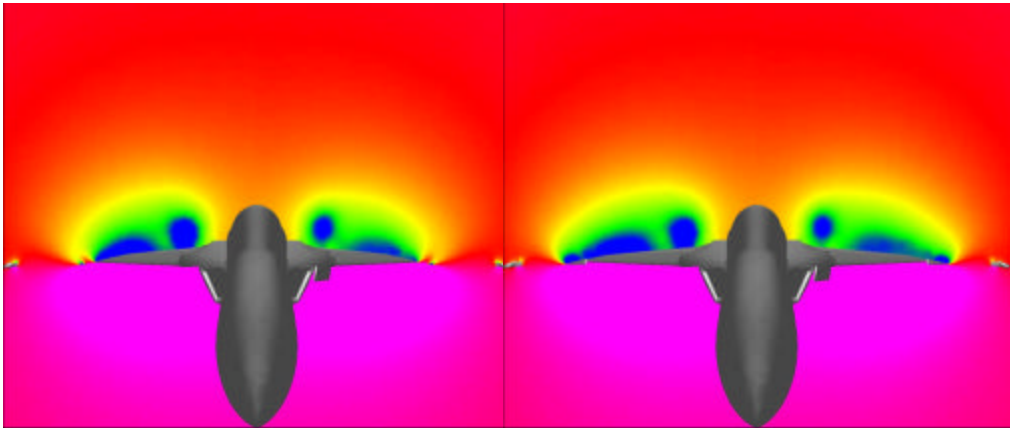
Frame 7

Frame 8



Frame 9

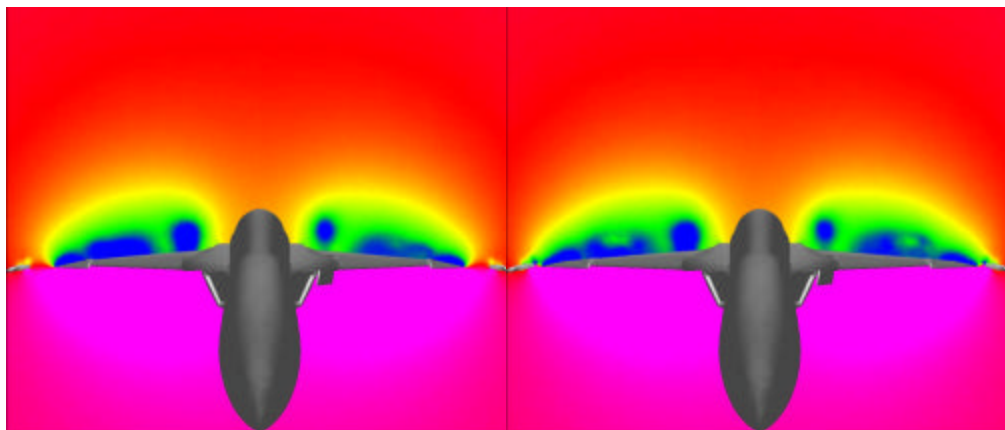
Frame 10



Frame 11

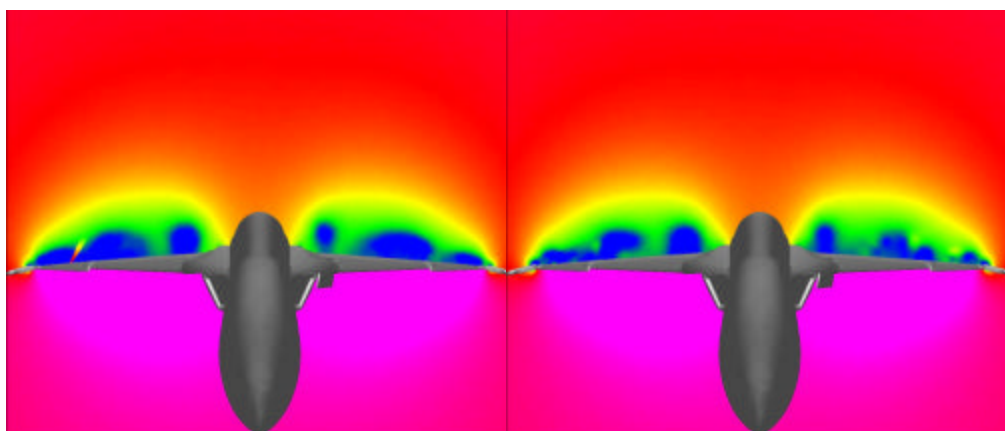
Frame 12

APPENDIX E



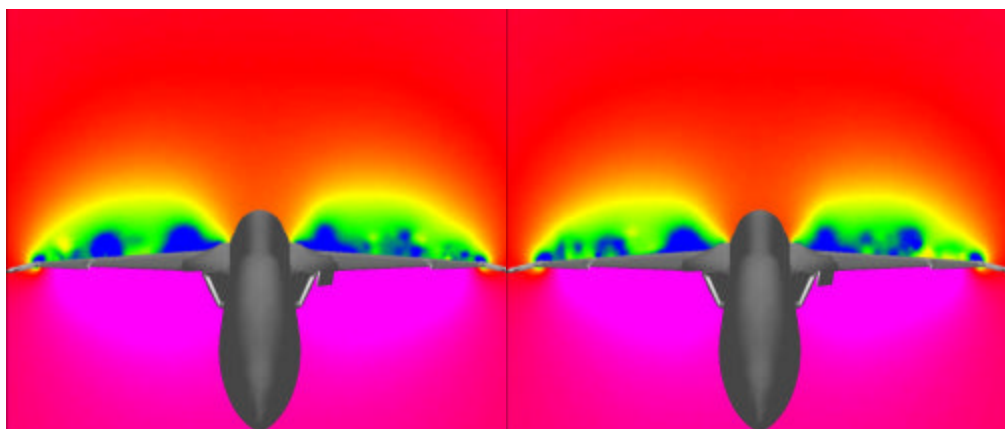
Frame 13

Frame 14



Frame 15

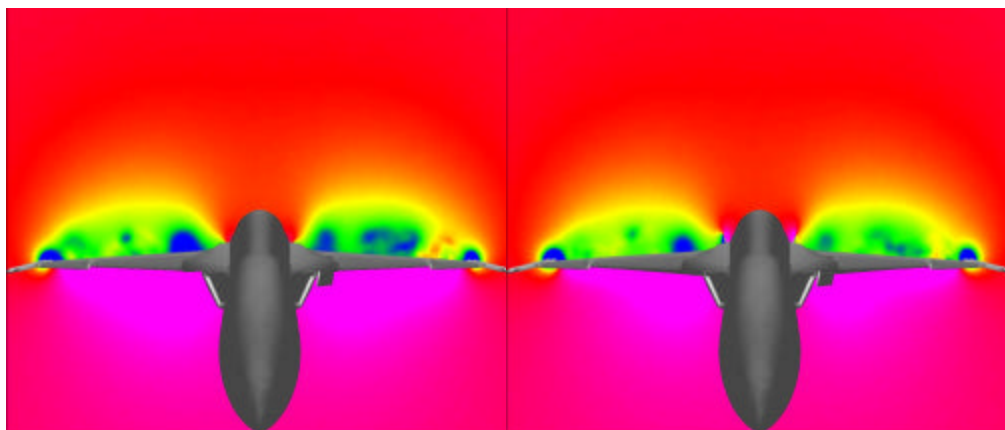
Frame 16



Frame 17

Frame 18

APPENDIX E

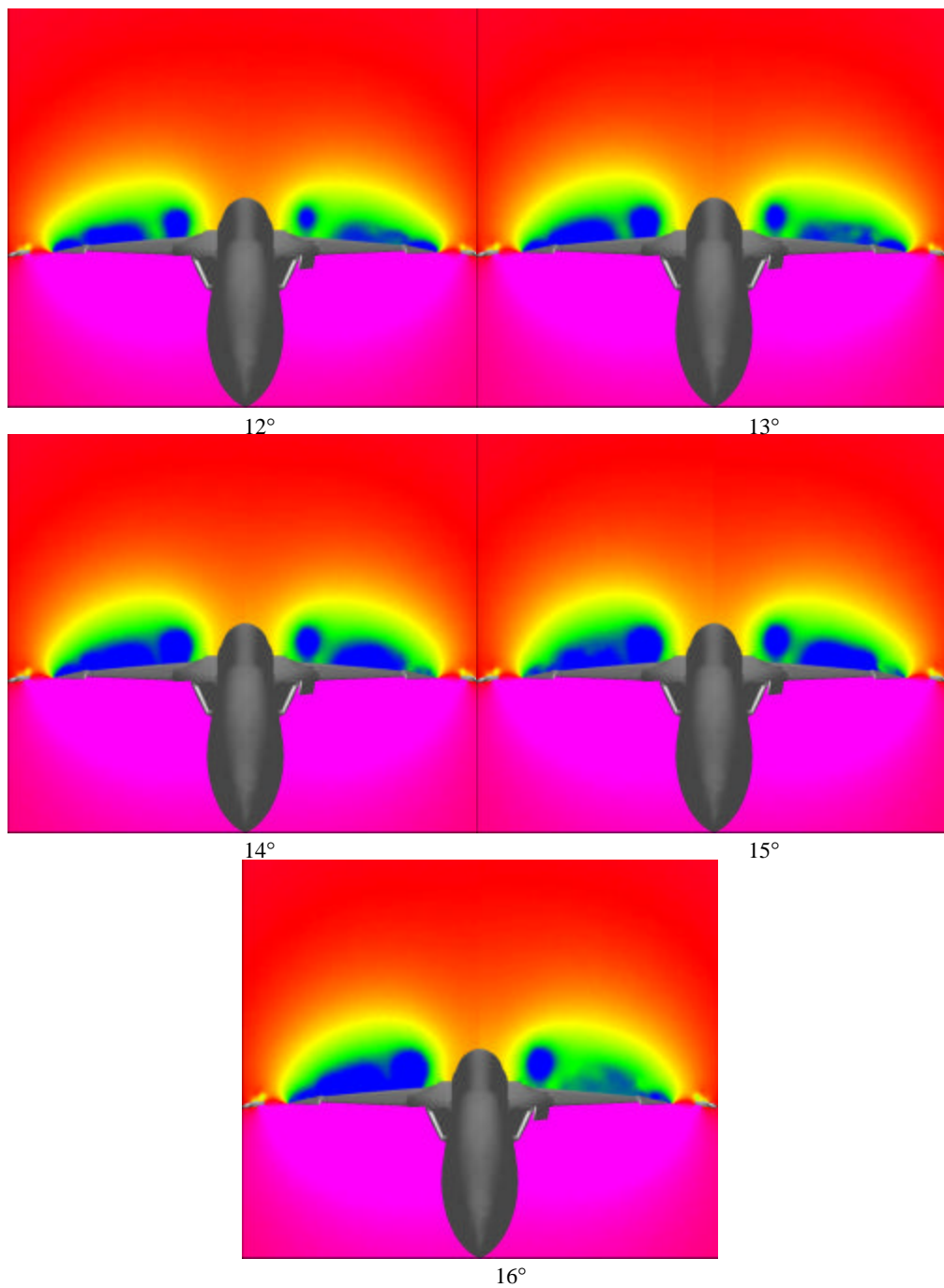


Frame 19

Frame 20

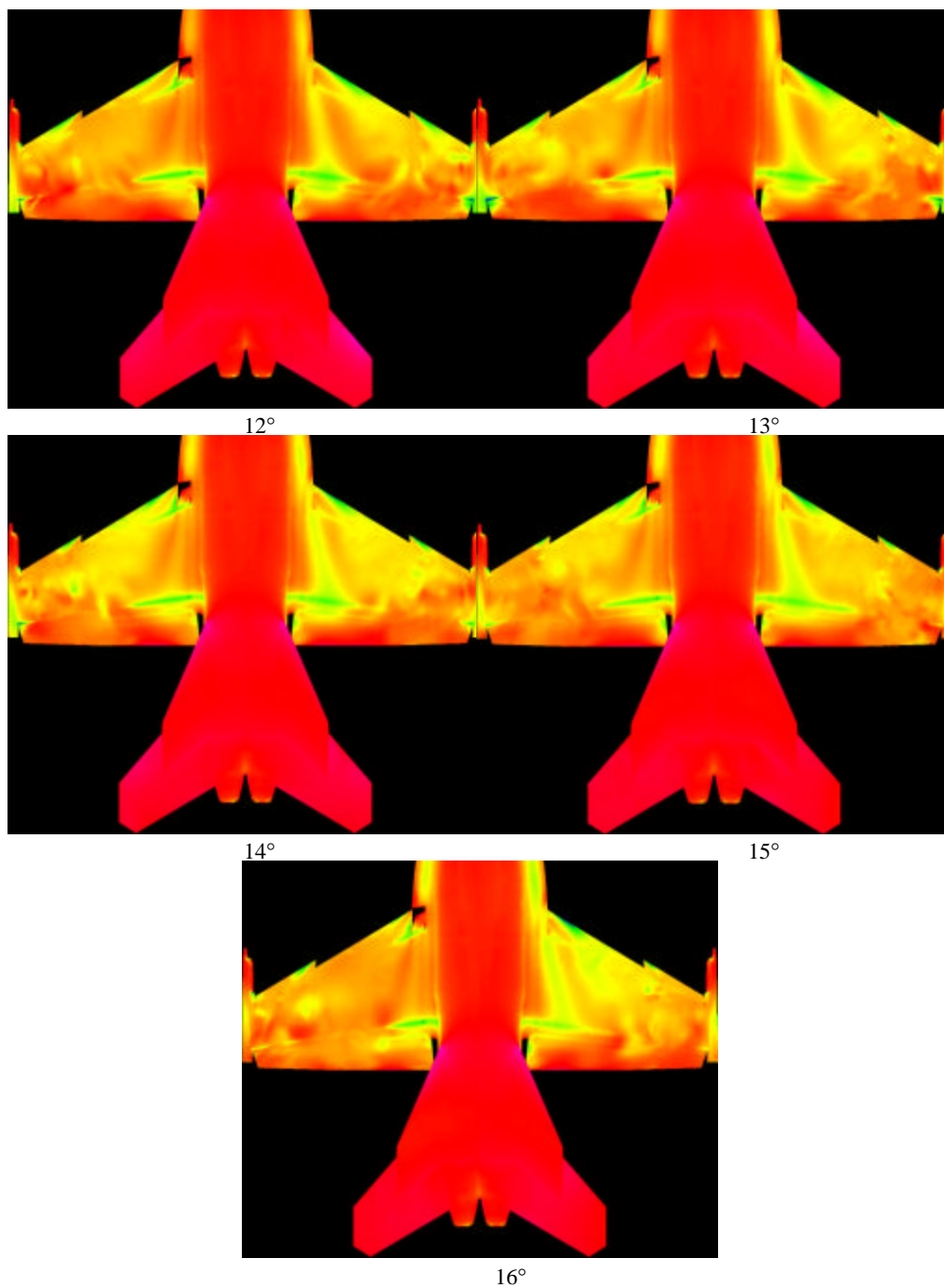
APPENDIX F

Animation Sequence Showing Angle-Of-Attack Progression At Constant Chord Location



APPENDIX G

Animation Sequence Showing Angle-Of-Attack Progression Of Surface Pressure Distribution



APPENDIX H

Animation Sequence Showing Angle-Of-Attack Progression
Of Surface Mach Number Distribution

